Received: 14 July 2020 | Revised: 17 November 2020 | Accepted: 23 November 2020

DOI: 10.1002/kin.21469

INTERNATIONAL JOURNAL OF CHEMICAL KINETICS WILEY

ARTICLE

Ignition delay and chemical–kinetic modeling of undiluted mixtures in a high-pressure shock tube: Nonideal effects and comparative uncertainty analysis

Lisa Zander | **Johann Vinkeloe** | **Neda Djordjevic**

Technical University of Berlin, Berlin, Germany

Correspondence
Lisa Zander, Technical University of Berlin, Berlin 10623, Germany.

Funding information
Deutsche Forschungsgemeinschaft, Grant/Award Number: 200291049

Abstract

High-pressure shock tube ignition delay data are essential for fuel characterization and for the validation and optimization of chemical–kinetic models. Therefore, it is crucial that realistic measurement conditions are considered in modeling. Furthermore, an accurate uncertainty quantification for experimental data is the basis for evaluation of the predictive reliability of chemical–kinetic models. Several measurement aspects are investigated to improve the interpretation of measurement results: (1) A new approach for integrating the nonideal pressure rise into chemical–kinetic modeling based on a correlation to measurement data is introduced, which enables the determination at each condition and fuel–air mixture individually with minimal effort. (2) A semiempirical model for available test times of reactive mixtures is introduced, which is based on measurement data of nonreactive mixtures. It allows for a priori prediction of test times and provides experimental limits to support the measurement. (3) A literature review shows that different uncertainty sources are considered in ignition delay time uncertainty analysis. A comparative analysis is conducted to investigate the significance of different uncertainty sources for test temperature and ignition delay time. The analysis of ignition delay time uncertainty indicates that for fuels with negative temperature coefficient behavior a comprehensive uncertainty analysis has to be conducted to accurately estimate measurement uncertainty in the intermediate temperature range. Additionally, ignition delay times of dimethyl ether–air mixtures are measured at pressures of 8, 12, and 35 bar and at equivalence ratios of 0.5, 1.0, and 2.0. Furthermore, the data on first-stage ignition delay are rather scarce and have therefore been recorded additionally. The new approach of integrating the nonideal pressure rise into modeling and the comprehensive uncertainty analysis supports the interpretation of measurement data, such that the prediction capabilities of chemical–kinetic models can be evaluated thoroughly.

List of abbreviations: DME, dimethyl ether; IDT, ignition delay time; ISW, incident shock wave; NTC, negative temperature coefficient; RSS, root sum of squares

KEYWORDS
dimethyl ether, ignition delay time, non-ideal effects, shock tube, test time, uncertainty analysis

1 | INTRODUCTION

Alternative synthetic fuels have the potential to partially replace conventional fossil fuels in the future. They can be designed to be environmentally compatible and reduce CO_2 emissions. Most synthetic fuels are thus far not conventionally used in combustion systems, and their combustion properties are not yet fully investigated. Hence, there is a large demand to characterize synthetic fuels with respect to their fundamental combustion properties, such as their ignition delay time (IDT).

Chemical–kinetic models describing hydrocarbon combustion are important to design and optimize combustion processes.[1] IDT represents one of the most important indirect experimental parameters used in combustion chemistry to validate and optimize detailed chemical–kinetic models due to its high sensitivity to major chain branching and termination reactions. Therefore, the fidelity and accuracy of such experimental data are essential.[2] Furthermore, to validate chemical–kinetic models at conditions relevant for practical applications, a database of IDTs of undiluted fuel–air mixtures at these conditions is essential.

In order to obtain IDTs for highly argon-diluted fuel–oxygen mixtures as well as undiluted fuel–air mixtures at practically relevant conditions, a new high-pressure shock tube facility is built. In a shock tube, a shock wave is generated, commonly by causing one or two diaphragms to burst due to the pressure difference imposed by a pressurized driver gas. The generated incident shock wave (ISW) travels through the test gas and reflects at the end of the test section, thereby compressing the test mixture nearly instantaneously to the desired measurement conditions achieved behind the reflected shock wave. The advantage of using a shock wave for compression of the test gas is that near instantaneous heating is achieved.[3, 4] However, there are certain challenges related to shock tube measurement of IDTs, such as nonideal effects, limited available test times, and a missing consensus on determining measurement uncertainties. The nonideal pressure rise is more severe for mixtures that are not highly diluted in argon, as it is larger in polyatomic bath gases.[5] Furthermore, the increased concentration of reactive species as well as the different bath gas species of fuel–air mixtures compared to highly argon-diluted mixtures may impact the uncertainty analysis with respect to which uncertainty components are significant. Hence, this publication examines theses aspects with focus on undiluted fuel–air mixtures. However, the methods developed in the scope of this publication can be applied to argon-diluted fuel–oxygen mixtures as well.

In an ideal experiment for IDT measurement, the gas state prior to ignition is constant throughout the test volume, such that chemical reactions are not affected by any changes in the thermodynamic state. However, in shock tube experiments, a nonideal rise in test pressure and temperature is observed in the test volume behind the reflected shock. It is caused by ISW attenuation originating from the boundary layer forming behind the ISW and nonideal shock formation due to opening of the diaphragms.[6] The attenuating ISW causes the state behind the ISW to be axially varying over the length of the shock tube. When the reflected shock compresses this postincident-shock gas with inhomogeneous state, pressure waves emerge and propagate into the test gas volume inducing a rise in test pressure and temperature.[6, 7] The nonideal temperature rise due to the boundary layer behind the ISW increases with increasing test temperature and decreasing test pressure.[6]

It was shown that not considering the nonideal temperature rise present in shock tube experiments can lead to significant errors in the activation energies of IDTs under certain conditions.[7] Neglecting the nonideal state change, which is present in the experiment, by applying the assumption of constant volume with constant internal energy in modeling can lead to misinterpretation of shock tube IDT data.[8] The nonideal change in the thermodynamic state of the test gas volume especially needs to be considered when measuring relatively long IDTs, as test temperature and pressure significantly increase with time.[6] A very recent publication deals with nonideal effects and their influence on chemical modeling, which underlines the relevance and topicality.[9]

Recently the nonideal state change is accounted for in chemical modeling. Commonly the experimentally recorded pressure trace is employed with the assumption of isentropic compression to determine the time-dependent compressed test gas state, for example, in CHEMSHOCK[10] or CHEMKINS SENKIN VTIM.[11] Chaos and Dryer[8] show that CHEMSHOCK and SENKIN VTIM deliver very similar results. As the nonideal pressure and temperature rise is facility dependent, it is necessary to investigate and report the nonideal rise in test pressure and temperature for each shock tube facility for successful modeling.[8] Postprocessing of the measured pressure trace with the aim of integrating it into modeling can be cumbersome, as noise and artificial components have to be removed for each individual measurement point. Usually, a single value is assumed for the nonideal pressure rise and used in modeling for a broad range of conditions, in order to compare chemical–kinetic model prediction to measurement data. However, it is difficult to choose a single nonideal pressure rise, which is valid for the whole investigated temperature range, as it increases with temperature, while its influence on IDT decreases with decreasing IDT and therefore increasing temperature. Furthermore, pressure and mixture composition influence the nonideal pressure rise. Thus, an improvement of how to integrate the nonideal state change into modeling is necessary.

The available test time in a shock tube facility is an important parameter, as it determines the lowest possible temperature for IDT measurements at a specific pressure for a specific test gas mixture. Test times in shock tubes are limited because either the initial expansion wave, which is generated through bursting of the diaphragm, or pressure waves reflecting from the contact surface after its interaction with the reflected shock wave propagate into the test volume and alter the test state.

There are cases where, depending on the measurement setup, it is not possible to distinguish whether a pressure increase before ignition above the nonideal pressure increase is caused by a reflected disturbance or chemical reactions. This is especially relevant for undiluted fuel–air mixtures with multistage ignition at low to intermediate temperatures, as first-stage ignition will result in a slight pressure increase of the test gas. It is possible to measure available test times of a test gas mixture by making it nonreactive by removing the fuel from the mixture. However, the larger fuel mole fraction in undiluted fuel–air mixtures significantly influences speed of sound and wave propagation. Therefore, test times will differ from the mixture without fuel used to determine the test times experimentally. Hence, a possibility to predict the available test time of a reactive gas mixture supports IDT measurements in shock tubes by helping to identify whether a reflected disturbance is the cause of a pressure change appearing before ignition.

Besides nonideal effects and limited test times, which can make the interpretation of shock tube IDT data difficult, IDT measurements are subject to uncertainty. As IDT is dependent on temperature, pressure, and mixture composition $\tau(T, p, X_i)$, the uncertainties in these quantities will propagate into IDT uncertainty, as well as uncertainties arising from the extraction of IDT from the measurement data itself. The indirect measurement procedure of test pressure and temperature (from ISW speed and the initial state), as well as the mixture preparation procedure, gives rise to uncertainties, which propagate into IDT uncertainty. Researchers determine uncertainties of measured IDTs differently, which complicates the assessment and comparison of IDT data between various data sources (compare Section 5). As precise knowledge of the accuracy of IDT data is essential for chemical mechanism development, the determination of uncertainty needs to yield comparable and valid results. The possibility of the neglection of certain uncertainty components needs to be investigated carefully.

To conclude, the accuracy of measurement data, such as IDTs measured behind reflected shock waves, is important for chemical–kinetic mechanism development and validation, especially data that replicate technically relevant conditions of undiluted fuel–air mixtures. However, nonideal effects, limited test times, and a missing consensus on determining measurement uncertainties pose a challenge for the evaluation of IDTs measured in shock tubes. Based on these challenges, when measuring IDTs of undiluted fuel–air mixtures at practically relevant conditions, the following goals are pursued in this work:

- Characterization of the nonideal facility dependent pressure rise of the new shock tube facility and development of an approach to determine the facility-specific pressure rise for each measurement condition automatically to be accounted for straightforward in modeling.
- Development of a simple semiempirical model to predict available test times for reactive test gases, in order to analyze influences on available test time and to support the experimenter in deciding when to dismiss a measurement.
- As there is no consensus for measurement uncertainty determination of IDTs, as detailed in Section 5 (compare Table 3), a comparative analysis of uncertainty components is provided. Various contributions to measurement uncertainty of test temperature and IDT depending on the measurement condition are investigated, with focus on undiluted fuel–air mixtures.
- New measurement data on IDTs of undiluted dimethyl ether (DME)–air mixtures of both first and overall ignition to extend the experimental data base on IDTs measured in shock tubes, which is less extensive for undiluted DME–air mixtures compared to argon-diluted DME–oxygen mixtures (compare Table 1), under consideration of nonideal effects and with in-depth measurement uncertainty.
- Additionally, a comprehensive comparison to prediction by kinetic models is performed for both first and overall measured IDTs, under consideration of nonideal effects and obtained uncertainties. DME is chosen because it is regarded as an alternative fuel and diesel substitute in compression-ignition engines.[33] Furthermore, the blending ratio of DME can be used for tailor-

TABLE 1 Reported IDTs of DME measured in shock tube (ST) and rapid compression machine (RCM)

ϕ	P (bar)	T (K)	First-stage ignition reported?	Facility	Reference
Highly diluted in argon					
0.5, 1, 2	3.5	1200–1600	no	ST	12
1, 2	1.8	1250–1540	no	ST	13
0.5, 1.0, 2.0	1.6-6.6	1175–1480	no	ST	14
1	1,5,10	1134–1576	no	ST	15
1	1.2, 5.3	1192–1670	no	ST	16
0.5, 1.0, 2.0	20	1085–1454	no	ST	17
0.5	2, 10, 20	1123–1647	no	ST	18
0.5, 1.0, 2.0	1.2, 10	1091–1532	no	ST	19
1.0	10	1166–1536	no	ST	20
0.5, 1.0, 2.0	1.2, 4.0, 10.0	1092–1643	no	ST	21
0.5, 1.0, 2.0	1.2, 4, 10, 20	1000–1600	no	ST	22
0.5, 1.0, 2.0	4, 10	987–1517	no	ST	23
0.5, 1.0, 2.0	20	1085–1456	no	ST	24
Diluted in nitrogen					
0.75, 1.5	10,15,20	615–735	yes	RCM	25
0.5, 1.0, 1.5;	22-23	1035–1202	no	ST	26
1.0	10	1291–1485	no	ST	20
1.0	35	845–1259	yes	ST	27
Measured in synthetic air					
1	13, 40	650–1300	yes	ST	28
0.43	10,15	615–735	yes	RCM	25
0.5, 1.0, 1.5;	23	697–1239	no	ST	26
0.3, 0.5, 1.0, 2.0	7-10, 11, 25, 30	651–1428	no	RCM, ST	29
1	30	602–645	no	RCM	30
0.5, 1.0	2, 10	650–1400	no	ST	31
0.3, 0.5	7,12,22	621–582	no	RCM	32
1.0	35	687–1057	yes	ST	27

ing IDT and its temperature sensitivity in fuel blends.[34] However, the investigation of shock tube performance is general and independent of the fuel and hence applicable to other alternative fuels.

2 | HIGH-PRESSURE SHOCK TUBE TEST FACILITY

2.1 | Design, hardware, and measurement procedure

A new high-pressure shock tube is designed and implemented (Figure 1). The design target is to measure IDTs of undiluted mixtures at conditions relevant to technical applications, such as internal combustion engine or gas turbine combustion. The maximum design pressure is 400 bar, whereas the test gas section can be heated up to 200°C with heating sleeves facilitating investigations with undiluted preevaporated liquid fuels as well. The shock tube has an inner diameter of 95 mm to reduce boundary layer effects, which are lower for large diameter shock tubes, since the blockage of the cross-section area by the boundary layer is reduced.[6] The effect of this choice of diameter on the nonideal pressure increase is investigated in Section 4.1. Additionally, the driven section surface is honed and electropolished to further decrease friction and thus boundary layer effects.

The shock tube is divided into two sections by the diaphragm housing chamber, the driver and the driven sections, each 6 m long. The long driven and diver section ensure that test times are sufficient for a range of temperatures even without applying methods, as for example, Refs. 35–37, for test time extension.

The shock tube can be operated in single or double diaphragm mode. In the scope of this work, prescored alu-

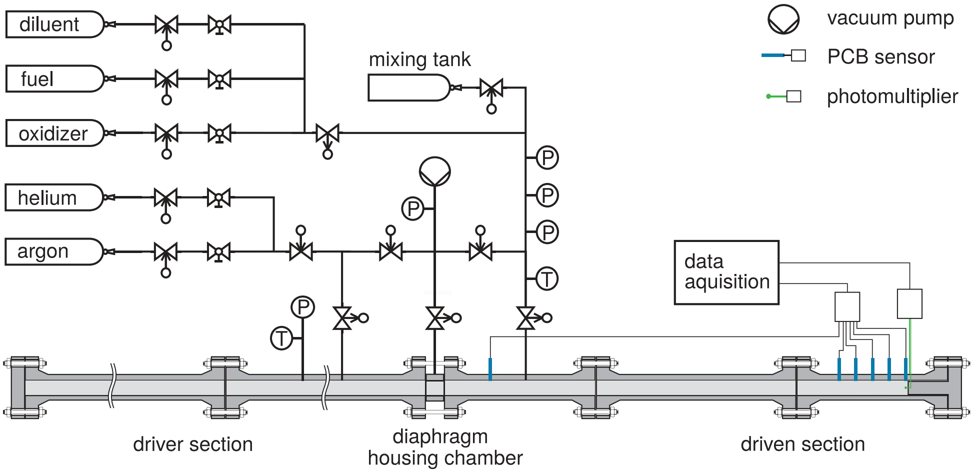

FIGURE 1 Schematic sketch of new high-pressure shock tube facility [Color figure can be viewed at wileyonlinelibrary.com]

minum diaphragms ranging from 0.3 to 1.5 mm thickness with a prescoring depth of 20–50% of the diaphragm thickness are used in a double diaphragm operation.

The ISW velocity is measured with five PCB-113B03 piezoelectric pressure sensors, which are axially distributed over the last 1.2 m of the shock tube. The distance between two adjacent sensors is 300.13, 299.66, 299.83, and 299.84 mm, with the last sensor being located at 3 mm from the end wall.

The pressure sensors are coated with high-temperature silicone, which is later referred to as shielded measurement, to reduce thermal shock behavior, where the rapid temperature increase by the shock leads to deformation of the pressure sensor housing and a falsely detected pressure decrease.[38] The coating ensures that the nonideal pressure rise is accurately detected when investigating nonideal effects.[6]

The incident of ignition can be determined with the piezoelectric pressure sensor that is closest to the end wall, since there is a significant pressure increase induced by the heat release from undiluted test gas mixtures. In the same axial plane as the pressure sensor, there are two quartz glass windows, which enable to measure chemiluminescence of ignition. Two Hamamatsu H10723-20 photomultiplier tubes are connected to the quartz glass windows by optical cables. Different optical filters can be positioned between the window and photomultiplier to measure chemiluminescence within a certain wavelength range only. For this publication, OH^* chemiluminescence is determined by using a filter centered around 309 nm to detect the main ignition event. Additionally, excited formaldehyde (CH_2O^*) emissions are recorded with a filter centered around 407 nm to detect the first stage of ignition, as already done in Ref. 39. Excited formaldehyde emission is observed during low-temperature oxidation of hydrocarbons.[40–42] Emission at 407 nm is within the broadband emission spectrum of formaldehyde.[40, 42, 43] Excited formaldehyde emission spectrum overlaps excited CH^* and C_2^*, but these species are not intrinsic to low-temperature oxidation.[43] Hence, emission at 407 nm can be associated with first-stage ignition.[39]

Chemiluminescence and pressure signals are recorded by a spectrum M2i4912-exp card with a data rate of 10 M samples/s into eight channels with a resolution of 16 bit. To reduce the size of the acquired data to the necessary only, the data acquisition is triggered by a piezoelectric pressure sensor (PCB-113B03) mounted in the driven section close to the diaphragm. An increase of the signal at this sensor over a certain threshold indicates that the diaphragm facing the driven section has ruptured, and pressure and chemiluminescence signals are recorded for a fixed duration of time.

The preshock condition of the test gas is measured by three MKS Baratron 121A absolute pressure transducers (121AA-00100B: 100 to 2×10^{-2} Torr, 121AA-05000B: 5.000 to 7×10^{-1} Torr, 121AA-20000B: 20,000 to 4 Torr) and a Pt100 resistance thermometer.

2.2 | Mixture preparation

To avoid uncertainty in mixture composition resulting from in situ mixture preparation for each measurement point, gas mixtures are prepared in a 50 l tank and are allowed to mix at least overnight. In this way, a whole measurement series is performed with the same mixture. In order to minimize the influence of mixture segregation and stratification, the tank is heated on one side prior to the experiment to induce a convective gas flow. Thus, the homogeneity of the mixture in the tank is increased, and it is ensured that a mixture with the desired composition is extracted from the tank when performing the experiments.

TABLE 2 Investigated gas mixtures

Mixture	ϕ	Mole fraction (%) of DME	O_2	N_2	Ar
M1	1.0	1.31	3.93	0.00	94.76
M2	0.5	3.30	19.82	76.87	0.00
M3	1.0	6.40	19.19	74.41	0.00
M4	2.0	12.02	18.04	69.94	0.00

Gas mixtures are prepared using the partial pressure method. The amount of gas filled into the gas cylinder is controlled through measuring the fill pressure with one of the three Baratron 121 pressure transducers.

Mixing tank, shock tube, and the gas-handling system are evacuated by a rotary vane pump below 2×10^{-4} bar. The vacuum pressure is measured by an Agilent RGC-100 rough gauge controller.

Four different gas mixtures are prepared for this work. Their composition is summarized in Table 2. Mixture M1 is a DME–oxygen mixture highly diluted in argon. It is prepared to resemble one measurement from Ref. 21 aiming at validation of the measurement method. Mixtures M2, M3, and M4 are mixtures of DME with synthetic air at equivalence ratios ϕ of 0.5, 1.0, and 2.0. Synthetic air is composed of 20.5 vol% oxygen and 79.5 vol% nitrogen with a mixture uncertainty of ±0.5%. The purity of the utilized gases is as follows: synthetic air, argon, and argon–oxygen greater than 99.999 mol% and DME greater than 99.99 mol%.

2.3 | Measurement data processing

The test gas state, as well as the IDT, is extracted from the data recorded during the measurement. According to the convention in shock-tube theory the state behind the reflected shock wave (the test state) is denoted with subscript 5, whereas the initial conditions in the driven section containing the combustion mixture to be investigated is denoted by 1.

The test gas state behind the reflected shock (T_5, P_5) is determined from the state before shock compression (T_1, P_1), the test gas composition, and the ISW velocity W_s. The ISW velocity is obtained from the arrival of the ISW at different axial locations in the shock tube, tracked by five piezoelectric pressure sensors (compare Figure 1). The time of arrival of the ISW at the sensor positions is obtained by finding the time of the local maximum pressure change. Due to nonideal effects, the ISW attenuates with increasing distance to the diaphragm. Therefore, the ISW velocity is extrapolated to determine its respective value at the end wall. A linear fit is chosen as it yields reasonable results even in the case of nonmonotonic ISW variations.[3]

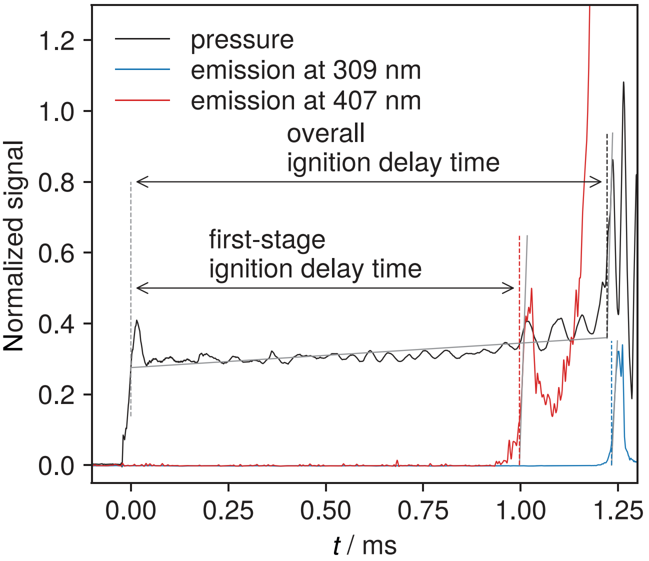

FIGURE 2 Extracting first-stage and overall IDT from measurement data [Color figure can be viewed at wileyonlinelibrary.com]

With the obtained ISW velocity and the state before shock compression (T_1, P_1), the test state (T_5, P_5) behind the reflected shock wave is determined by solving mass, momentum, and energy equation over the incident and reflected shock wave. It is assumed that the composition of the test gas remains constant after shock compression. The solution algorithm is implemented in Python. The thermochemical properties of the species in the test gas are taken from a chosen chemical–kinetic model and are integrated into the solution algorithm through the open-source software package cantera.[44] It is assumed that the test gas behaves like an ideal gas. Due to the object-oriented implementation of the solution algorithm, it can be easily applied to real gases as well. However, for the present study, the error due to the ideal gas assumption is determined as negligible (compare Section 5.1).

IDT is defined as the time between the passage of the reflected shock through the measurement plane and the moment of ignition. A linear function is fitted to the section of the pressure signal between the pressure increase caused by the reflected shock and the increase due to heat release of ignition (Figure 2). The beginning of IDT equals the intersection of this function with the pressure signal at the instance of the passage of the reflected shock (Figure 2). For DME–air mixtures (M2–M4), the moment of ignition is determined from the pressure time history as the time of intersection of this linear function and the extrapolated maximum pressure gradient (Figure 2). When measuring IDT of argon-diluted mixtures, the moment of ignition is additionally determined by extrapolation of the maximum slope of the OH* chemiluminescence emission signal at 309 nm to the zero signal level. Note that overall IDT is similar between OH* and the pressure trace. Additionally, first-stage IDT is extracted from the CH_2O^* chemiluminescence signal measured at 407 nm, again by extrapolation of the maximum slope to the zero-signal level.

3 | NUMERICAL METHOD

IDTs are predicted with a homogeneous constant volume reactor using the open-source software package cantera.[44] Additionally, simulations with a variable volume reactor are performed, which take into account the nonideal pressure and temperature rise occurring in the experiment. The prescribed time-dependent volume is determined from the nonideal pressure rise assuming isentropic compression. The following set of differential equations is solved:

$$\frac{dY_i}{dt} = \frac{M_i}{\rho} \sum_{j=1}^{N_r} \nu_{ij} r_j \tag{1}$$

$$\rho c_v \frac{dT}{dt} = \frac{1}{\gamma} \frac{dP_5}{dt} - \sum_{i=1}^{N_s} \sum_{j=1}^{N_r} \nu_{ij} r_j u_i \tag{2}$$

$$\frac{dv}{dt} = -\frac{1}{\gamma} \frac{v_0}{P_{50}} \frac{dP_5}{dt} \tag{3}$$

with Y_i and M_i denoting the ith species mass fraction and molar mass, ρ the density, c_v the specific heat capacity at constant volume, $\frac{dP_5}{dt}$ the nonideal pressure rise, ν_{ij} the stoichiometric coefficient of species i in reaction j, r_j the rate-of-progress variable of reaction j, γ the ratio of specific heats, u_i the ith species molar internal energy, N_s the number of species, and N_r the number of reactions, with v_0 and P_{50} denoting the initial specific volume and pressure at the beginning of the simulation, that is behind the reflected shock wave. The set of Equations (1)–(3) is implemented in Python with the software package cantera and solved with the RADAU solver[45] for stiff differential equation systems.

In the experiment, the nonideal pressure rise depends on the measurement condition and mixture. Multiple DME–air mixtures are investigated at different pressures and temperatures, as provided in Section 6. In this work, the nonideal pressure rise is determined based on a correlation to measurement data with the aim to replicate the nonideal pressure rise at each exact measurement condition with minimal effort for the investigated DME–air mixtures. Thus, rather than assuming the same pressure rise for each condition and mixture, the nonideal pressure rise is determined for each point individually. Details on the measurement of the nonideal pressure rise are provided in Section 4.1 ,and the measured nonideal pressure rise is presented in Figure 5. With linear regression, a correlation for the nonideal pressure rise of synthetic air mixtures is obtained from the measurement data (Figure 5),

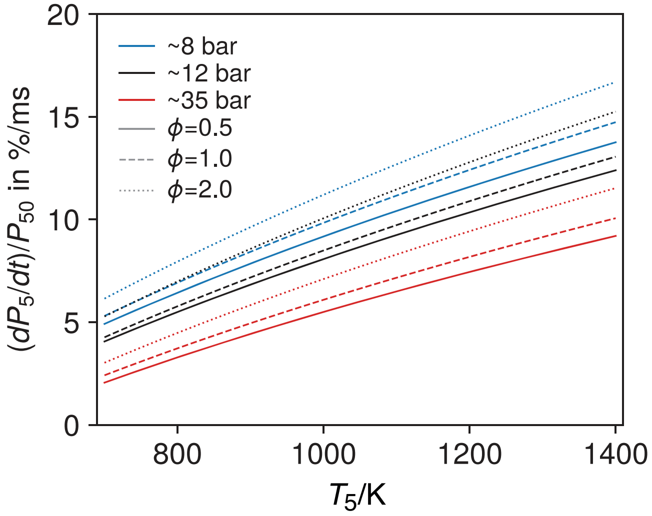

FIGURE 3 Nonideal pressure rise for DME–air mixtures at different equivalence ratios and test pressures used in the variable volume simulations [Color figure can be viewed at wileyonlinelibrary.com]

$$\frac{dP_5}{dt} \frac{1}{P_{50}} = \left(9.56 M_S^{0.5} P_1^{-0.14} - 9.96\right) \frac{\%}{\mathrm{ms}}. \tag{4}$$

The Mach number and initial pressure scaling in correlation (4) are chosen analogous to viscous ISW attenuation.[6, 46] For calculating the nonideal pressure rise with correlation (4) at each investigated condition and mixture composition, the ISW Mach number M_s and initial pressure P_1 are determined through solving the conservation equations. Thus, the correlation is also applied for fuel–air mixtures.

The in this way determined nonideal pressure rise increases with increasing temperature, decreasing pressure, and increasing fuel content (Figure 3). The temperature dependency and fuel content dependency of the modeled pressure rise is based on the Mach number, that is for higher temperatures and higher fuel contents a higher Mach number is necessary. Thus, the presented model reflects the strong relation between the nonideal pressure rise and Mach number observed by other researchers as well.[5, 9, 47] The pressure dependency is caused by the effect of a change in density on Reynolds number and therefore boundary layer growth.[5]

Different chemical–kinetic models are employed in the simulations. Details are provided in Section 6. The IDT of the main ignition stage is determined from the simulated pressure time history the same way as with measurement data. As excited CH_2O^* is not included in the investigated chemical–kinetic models, the maximum gradient of first-stage temperature increase is extrapolated to the initial temperature to determine the first-stage IDT.

4 | PERFORMANCE OF THE HIGH-PRESSURE SHOCK TUBE FACILITY

4.1 | Nonideal effects

To assess the performance of the new shock tube, nonreactive measurements are performed for argon and synthetic air test gases using a helium driver gas. The facility-specific ISW attenuation and nonideal pressure and temperature rise in the measurement plane are determined. For this purpose, nonreactive measurements are chosen to exclude the possibility of a pressure rise appearing due to heat release from chemical processes and assess only the pressure rise due to nonideal effects, as this is the common procedure, for example, Refs. 6 and 46.

The nonideal pressure rise is determined by performing a linear regression on the constant slope section of the pressure signal in the measurement plane after the passage of the reflected shock (Figure 1 in the Supporting Information). The nonideal temperature rise $\frac{dT_5}{dt}$ can be inferred from the measured pressure rise $\frac{dP_5}{dt}$ by assuming an isentropic relation between both[6] as follows:

$$\frac{dT_5}{dt} \approx \frac{T_{50}}{P_{50}} \frac{(\gamma(T_{50})-1)}{\gamma(T_{50})} \frac{dP_5}{dt}, \tag{5}$$

where T_{50}, P_{50} are the pressure and temperature just after the passage of the reflected shock and $\gamma(T_{50})$ is the heat capacity ratio of the test gas at these conditions. ISW attenuation $\frac{dW_s}{dx}$ is determined from linear regression of the axial variation of the ISW speed over the last 1.2 m of the shock tube test section.

Please note that a big fraction of the measurements with the argon test gas is performed with unshielded pressure transducers, which might lead to some inaccuracy in the detected pressure rise. Nevertheless, ISW attenuation measurements are not affected by the application of thermal silicone to the sensors, since these are only based on time-of-flight measurements. Therefore, incident shock attenuation is compared for the measurements with argon test gas to data from Petersen et al.[6] in Figure 4. ISW attenuation dW_s/dx is normalized to the ISW speed at the end wall W_{s0}. Figure 5 compares the nonideal pressure and temperature rise measured in synthetic air to data from Ref. 46 and measured in argon to data from Ref. 6. Pressure and temperature rise are normalized to their respective values just after the passage of the reflected shock. Note that the nonideal pressure rise in Ref. 46 is obtained with a shielded pressure sensor. In Ref. 6, the nonideal pressure rise is derived from IR-emission signal, as well as shielded pressure measurement. The data in Figures 4 and 5 are presented over $M_s^{0.5}P_1^{-0.14}$, because ISW attenuation due to viscous effects scales with the ISW Mach number and pressure as $M_s^{0.5}P_1^{-0.14}$ accordingly,[6, 9] while nonideal pressure and temperature rise are functions of incident shock attenuation.[48]

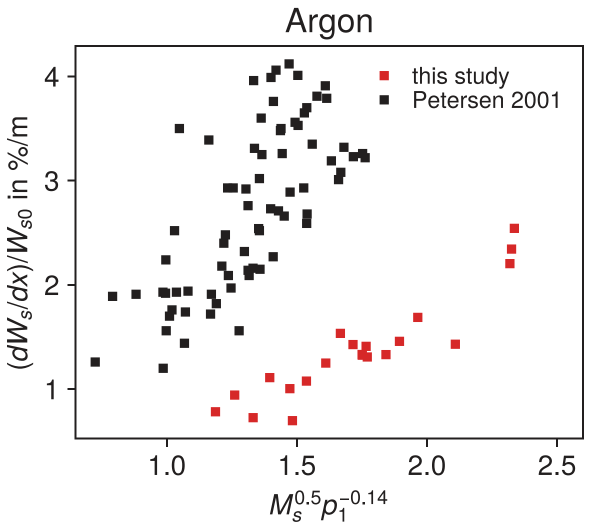

FIGURE 4 Incident shock attenuation for argon test gas compared to data from Ref. 6 [Color figure can be viewed at wileyonlinelibrary.com]

ISW attenuation values measured in the new high-pressure shock tube are significantly lower than the ones measured in Ref. 6. The reason for that is that the inner diameter of the present shock tube is almost twice as big as the one of the shock tube used in Ref. 6, which has an internal diameter of 50 mm. Smaller shock tube diameters lead to higher nonideal effects, due to a greater blockage of the shock tube cross-section area by the boundary layer.[6] The performance of the new shock tube is comparable to that in Ref. 46, as can be seen from the similar nonideal pressure and temperature rise in Figure 5, even though the shock tube used in Ref. 46 has a significantly larger internal diameter of 140 mm. This indicates that the blockage of the internal diameter by the boundary layer becomes insignificant at a certain internal diameter and supports the computational finding in Ref. 6 that the influence of the shock tube diameter on the nonideal temperature rise decreases with increasing diameter. Thus, a cost-intensive further increase in the internal diameter might not lead to significant improvements in shock-tube performance.

4.2 | Available test times

For the new shock tube, test times are determined experimentally for argon and synthetic air test gases. Test times

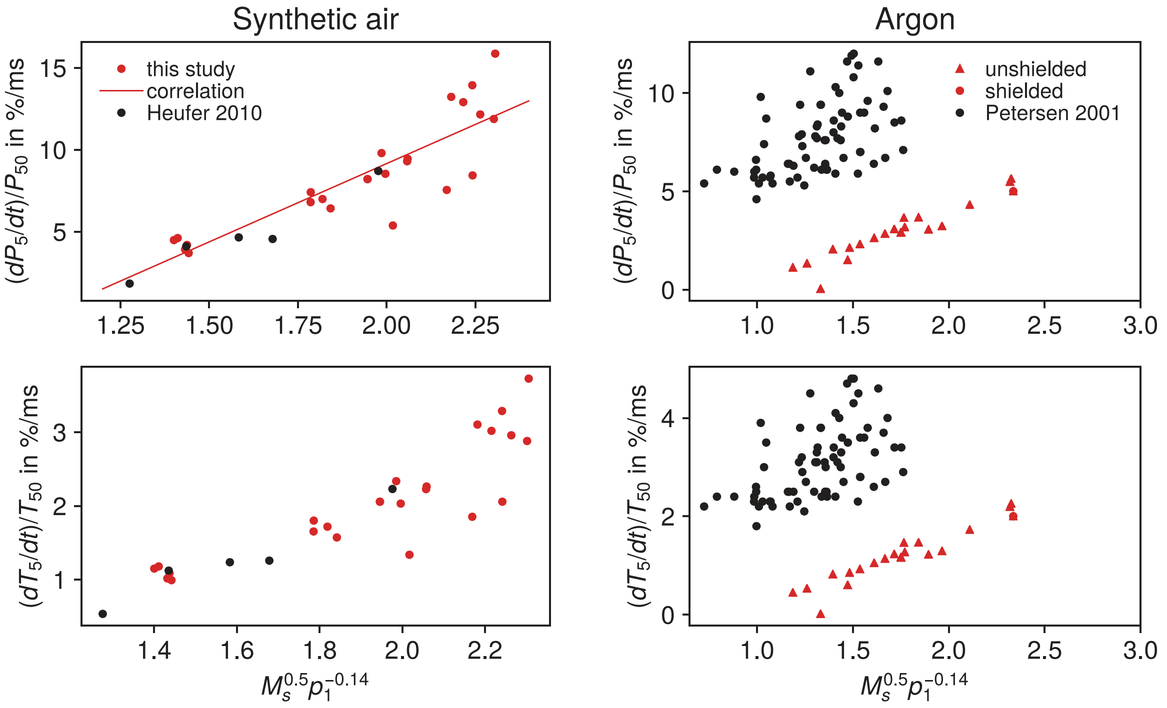

FIGURE 5 Comparison of nonideal pressure rise to other facilities for synthetic air (left, compared to data from Ref. 46) and argon (right, compared to data from Ref. 6) test gas [Color figure can be viewed at wileyonlinelibrary.com]

are defined starting from the instance of the passage of the reflected shock through the measurement plane until the instant, when the slope of the pressure signal deviates from the slope caused by ISW attenuation (Figure 1 in the Supporting Information).

As it is difficult to measure available test times of fuel–air mixtures over a broad range of test temperatures, a model with ideal shock tube behavior is implemented, which will be referred to as *ideal model* in the following. It calculates the available test time t_t from the interactions of waves in the shock tube considering the length of the driven section L (Figure 6). The ideal model only considers the case that the test time is limited by reflections arising from the interaction of contact surface and reflected shock, as the shock tube's relatively long driver section ensures that the initial expansion wave arrives at the measurement plane relatively late for test conditions relevant for IDT measurement. Constant wave propagation velocities are assumed, that is constant ISW velocity W_s, constant reflected shock velocity W_r, and constant propagation velocity of the contact surface u_2 and reflected disturbance u_d. Furthermore, it is assumed that the reflected disturbance travels at the speed of sound in region 5. The beginning of the test time t_0 equals

$$t_0 = \frac{L}{W_s}. \tag{6}$$

The instance when the reflected disturbance arrives at the end wall t_2 and terminates the test time is given by

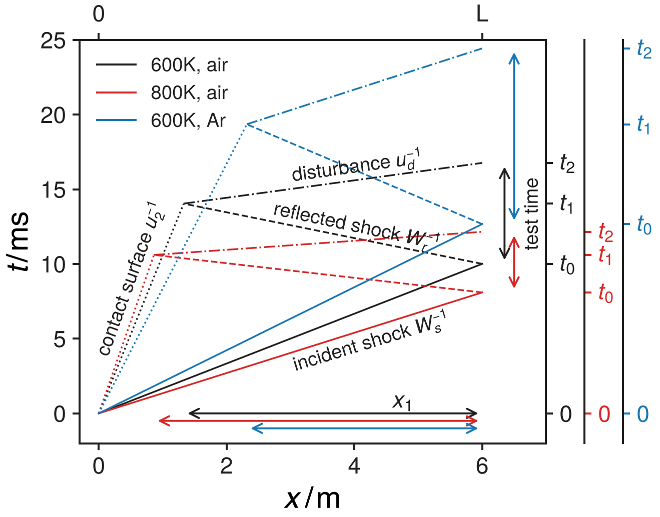

FIGURE 6 Influence of test gas and test temperature on wave propagation in an ideal shock tube [Color figure can be viewed at wileyonlinelibrary.com]

$$t_2 = L\left(u_d^{-1} + \frac{W_s^{-1} + W_r^{-1}}{u_2^{-1} + W_r^{-1}}(u_2^{-1} - u_d^{-1})\right). \tag{7}$$

The test time t_t is equal to

$$t_t = t_2 - t_0. \tag{8}$$

Figure 7 shows the measurement results in comparison to ideal model prediction. It can be seen that avail-

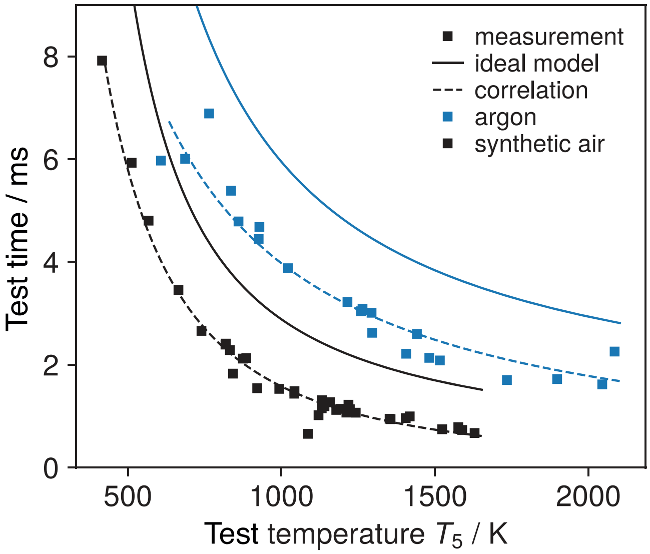

FIGURE 7 Measured test times for synthetic air and argon in comparison to the prediction by the ideal model [Color figure can be viewed at wileyonlinelibrary.com]

able test times decrease with increasing test temperature, as the ISW velocity, reflected shock velocity, contact surface propagation velocity, and speed of sound in region 5 increase. This is as well illustrated in Figure 6. The distance x_1 between the end wall and the location of the interaction of reflected shock and contact surface increases with increasing test temperature, as the velocities of incident, reflected shock, and contact surface do not increase with test temperature at the same rate (compare black curve – 600 K to red curve – 800 K). Even though x_1 increases, both the time $t_1 - t_0$ between the beginning of the test time and the interaction of contact surface and reflected shock, and $t_2 - t1$, the time it takes the reflected disturbance to travel back to the end wall, decrease with increasing test temperature. The cause of the former is that the propagation velocity of the contact surface increases stronger with increasing temperature than the velocity of the reflected shock. The latter is due to the stronger increase in speed of sound in region 5 compared to the increase in the distance x_1 the disturbance has to travel back.

Available test times in argon are longer than in synthetic air because of its different properties, that is a higher molar mass and heat capacity ratio (Figure 7), resulting in the same test temperature T_5 being achieved with a lower ISW velocity. This manifests in a steeper slope of the trajectory of the ISW in the x–t diagram in Figure 6 (compare black curve – air to blue curve – argon). The resulting wave velocity of the reflected shock is slower as well, which leads to an increase in $t_1 - t_0$. Because of the lower ratio of heat capacity ratio to molar mass in argon, the speed of sound is lower compared to air at the same temperature T_5. As a result, the disturbance travels back from the contact surface to the measurement plane at a lower speed. Even though x_1 is reduced as well, the decrease in reflected shock velocity and speed of sound prevails leading to an increased time $t_2 - t_1$.

Test times predicted by the ideal model are longer than measured test times (Figure 7), because the ideal model does not consider the effects of ISW attenuation, which also causes the contact surface to accelerate. Due to the deviation between ideal model and measurement, the ideal model can only be applied with modification to determine test times a priori, for example, for undiluted fuel–air mixtures. This can, for example, be achieved by considering a model accounting for viscous effects.[49] However, this requires the development of more complex models, which are subjected to uncertainty as well. Instead, in the present study a semiempirical easy-to-implement approach is proposed. In the following, test times measured in nonreactive mixtures are used to estimate test times of fuel–air mixtures. The deviation between the ideal model prediction and experimental test times, which is caused by the neglection of nonideal effects, is described by a mapping function $F(T_5)$, which is based on test time measurements of nonreactive mixtures (in this case synthetic air),

$$F(T_5) = \frac{t_{t,\,\mathrm{exp,\,air}}(T_5)}{t_{t,\,\mathrm{ideal,\,air}}(T_5)}, \tag{9}$$

with $t_{t,\,\mathrm{exp,\,air}}$ being the correlation to the measured test times in synthetic air and $t_{t,\,\mathrm{ideal,\,air}}$ being the respective ideal model prediction. To obtain an estimate of the experimental test times of fuel–air mixtures $t_{t,\,\mathrm{exp,\,DME/air}}(T_5)$, the mapping $F(T_5)$ is then applied to the prediction of test times by the ideal model $t_{t,\,\mathrm{ideal,\,DME/air}}(T_5)$ for fuel–air mixtures,

$$t_{t,\,\mathrm{exp,\,DME/air}}(T_5) \approx F(T_5) \cdot t_{t,\,\mathrm{ideal,\,DME/air}}(T_5). \tag{10}$$

Figure 8 depicts the ideal model predictions for synthetic air and DME–air mixtures with equivalence ratios of $\phi = 1$ and $\phi = 2$ together with the estimate of experimental test times. Note that the estimate of the test time of synthetic air is equal to the correlation based on measured test times. Also shown are measured test times for DME–air mixtures, which are extracted from pressure traces where no ignition occurred within the recording time or an expansion wave arrived at the measurement plane prior to ignition. Using only cases where an expansion wave arrives at the measurement plane ensures that cases are excluded where the first ignition stage (or premature ignition) can be misinterpreted as a pressure wave originating from the interaction of reflected shock and contact surface. Both the ideal model and the estimate of experimental test times reflect that the greater the mole fraction of fuel in the mixture the

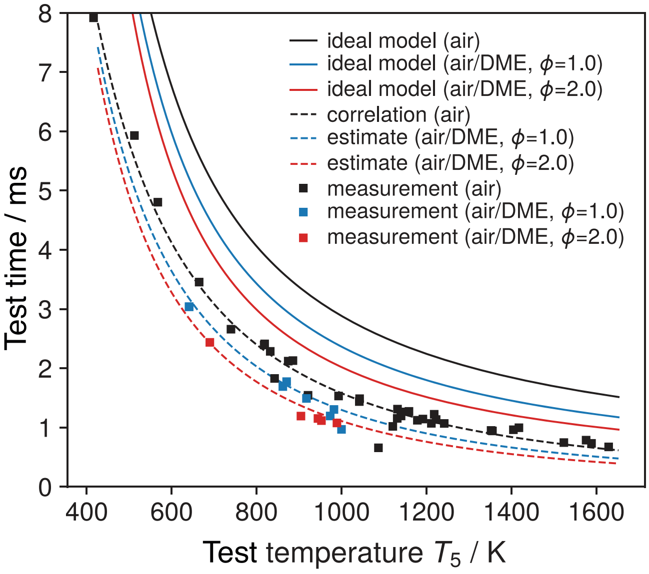

FIGURE 8 Prediction of test times by ideal model (Equations (6)–(8)) and estimate of test times (Equation 10) in comparison to measured test times of synthetic air and DME–air test gases [Color figure can be viewed at wileyonlinelibrary.com]

shorter the test time. The agreement between the estimate of the experimental test times of DME–air mixtures and their respective measurements is very good. Hence, test times of reactive mixtures in shock tubes can be successfully predicted with the help of a simple mapping approach based on test time measurements of nonreactive mixtures of similar composition. The required mapping function can be determined without additional costs from nonreactive measurements, which need to be acquired in any case in order to determine the performance curve (i.e., driver-to-driven pressure ratio over ISW Mach number[48]) for measurement planning, as well as characterize the facility-specific pressure increase.

5 | UNCERTAINTY ANALYSIS

Based on a literature survey, it appears that there is no consensus among researches with respect to uncertainty determination of IDT yet. Different approaches for uncertainty determination are exemplary summarized in Table 3.Multiple uncertainty sources are considered for measured IDT. Table 3 also lists uncertainty components for test temperature and pressure, as they propagate into IDT uncertainty.

While the test temperature T_5 is considered as an uncertainty cause for IDT in all studies (Table 3), the determination of test temperature uncertainty differs in the literature. Petersen et al.[3] determine the uncertainty in test temperature based on the uncertainty in ISW velocity W_s arising from the measurement procedure. While this approach is used by other researchers with similar ISW velocity measurement setups to also determine the uncertainty in test temperature, for example, Refs. 21, 57, 63 occasionally even the uncertainty in IDT is determined based solely on ISW velocity uncertainty.[21] Additionally to the uncertainty in ISW velocity W_s, the measurement uncertainties in incident temperature T_1 and composition X_i are considered as uncertainty components for test temperature.[52, 56] Other researches attribute the uncertainty in test temperature to nonideal effects and preignition pressure rise and neglect the influence of uncertainties arising from the measurement setup.[42, 53, 54] In Ref. 52, test temperature uncertainty is determined from both, the uncertainty caused by the measurement setup and the variation due to nonideal effects.

Some researchers estimate the uncertainty in IDT from the uncertainty in test temperature T_5 solely, for example, Refs. 21, 50, 53, 58. Additionally, the uncertainty of the pressure P_5 behind the reflected shock,[51, 54, 57] as well as the uncertainty in initial test gas composition X_i, are considered for IDT uncertainty.[26, 52, 56, 62] Similar to the uncertainty in test temperature, the uncertainty in test pressure is determined from one or multiple components arising from uncertainties in the initial conditions (P_1, T_1), ISW speed W_s and composition X_i, as well as nonideal effects and preignition. Except for Ref. 56, it is not described how the uncertainty in mixture composition is obtained in the literature listed in Table 3. Shao et al.[62] also include an uncertainty component arising from the choice of the equation of state (EOS). Furthermore, the uncertainty of extracting the IDT from the recorded pressure and chemiluminescence time histories,[26, 59, 61, 62] as well as an uncertainty component due to different IDT definitions,[51, 52, 62] are also included as contribution to IDT uncertainty by some researchers.

These different approaches for IDT uncertainty determination make it difficult to compare and interpret measurement data. In the following, a comparative analysis of different uncertainty contributions to test temperature and IDT is performed at various conditions aiming at analyzing the effect of their neglection on the reported uncertainty.

5.1 | Determination of uncertainties for measurement of IDT

The determination of uncertainties is performed according to the guidelines of the Joint Committee for Guides in Metrology.[64] In this study, uncertainties are always presented based on an interval of three standard deviations, as this will provide an interval where the actual measurement value is included with great likelihood (99.7%). This

TABLE 3 Different approaches of uncertainty analysis in literature

Components of T_5 uncertainty					Components of P_5 uncertainty						Components of IDT uncertainty						
T_1	W_s	X_i	Nonideal effects	Preignition	P_1	T_1	W_s	X_i	Nonideal effects	Preignition	T_5	P_5	X_i	Extraction	Definition	EOS	Ref.
N/S	N/S	N/S	N/S	N/S	–	–	–	–	–	–	+	–	–	–	–	–	50
–	+	–	–	–	–	–	+	–	–	–	+	+	–	–	+	–	51
+	+	+	+	–	+	+	+	+	+	–	+	+	+	–	+	–	52
–	–	–	+	–	–	–	–	–	–	–	+	–	–	–	–	–	53
–	–	–	+	+	–	–	–	–	+	+	+	+	–	–	–	–	54
–	+	–	–	–	–	–	–	–	–	–	+	–	–	–	–	–	55
–	–	–	+	+	–	–	–	–	–	–	not determined						42
+	+	N/S	–	–	+	+	+	N/S	–	–	+	+	+	+	–	–	26
+	+	+	–	–	+	+	+	+	–	–	+	+	+	–	–	–	56
–	+	–	–	–	–	–	–	–	–	–	+	–	–	–	–	–	21
–	+	–	–	–	N/S	N/S	N/S	N/S	N/S	N/S	+	+	–	–	–	–	57
N/S	N/S	N/S	N/S	N/S	–	–	–	–	–	–	+	–	–	–	–	–	58
–	+	–	+	–	–	–	–	–	–	–	+	–	–	+	–	–	59
N/S	N/S	N/S	N/S	N/S	–	–	–	–	–	–	+	N/S	N/S	N/S	N/S	N/S	60
–	+	–	–	–	–	–	–	–	–	–	+	–	–	+	–	–	61
N/S	N/S	N/S	N/S	–	N/S	N/S	N/S	N/S	+	–	+	+	+	+	+	+	62
+	+	+	–	–	+	+	+	+	–	–	+	+	+	+	–	–	this study

+ - component considered, – - component not considered, N/S - not specified interval is chosen wider than in the analyzed literature (e.g., two standard deviations in Ref. 62), where it is however mostly not provided. Nonideal effects are not considered in the uncertainty analysis, as they are included in the chemical modeling, as described in Section 3. Furthermore, an uncertainty due to the definition of IDT is not accounted for, as the utilized experimental definition is explicitly stated and can be replicated in modeling. An uncertainty component due to the choice of the equation of state when determining the test state is also not considered, as it is negligible for the investigated test pressures.[65, 66]

The uncertainty of the measured gas state before shock compression ($u(T_1), u(P_1)$), as well as the uncertainty in ISW velocity $u(W_s)$, propagates into the uncertainty of the test gas state, as it is determined by solving the conservation equations over incident and reflected shock based on the state and composition of the gas before shock compression and the shock velocity. The uncertainty in test temperature $u(T_5)$ and pressure $u(P_5)$ is estimated with the law of uncertainty propagation,[64]

$$u(T_5) = \sqrt{\left(\frac{\partial T_5}{\partial T_1}\right)^2 u^2(T_1) + \left(\frac{\partial T_5}{\partial W_s}\right)^2 u^2(W_s) + \sum_{i=1}^{N}\left(\frac{\partial T_5}{\partial X_i}\right)^2 u^2(X_i)}, \tag{11}$$

$$u(P_5) = \sqrt{\left(\frac{\partial P_5}{\partial P_1}\right)^2 u^2(P_1) + \left(\frac{\partial P_5}{\partial T_1}\right)^2 u^2(T_1) + \left(\frac{\partial P_5}{\partial W_s}\right)^2 u^2(W_s) + \sum_{i=1}^{N}\left(\frac{\partial P_5}{\partial X_i}\right)^2 u^2(X_i)}. \tag{12}$$

The sensitivity functions $\frac{\partial T_5}{\partial T_1}, \frac{\partial T_5}{\partial W_s}, \frac{\partial T_5}{\partial X_i}$ in Equation (11) and $\frac{\partial P_5}{\partial P_1}, \frac{\partial P_5}{\partial T_1}, \frac{\partial P_5}{\partial W_s}, \frac{\partial P_5}{\partial X_i}$ in Equation (12) are evaluated numerically using a central difference scheme. The uncertainty of the pressure and temperature measurement before shock compression ($u(T_1), u(P_1)$) is determined from all the components in their respective measurement chain. The uncertainty of test gas composition $u(X_i)$ is determined from the uncertainties of the pressure measurement due to mixture preparation with the partial pressure method and an uncertainty component that takes into account nonperfect vacuum in the mixing tank and shock tube. The estimation method for mole fraction uncertainties of the test gas species and the uncertainty in equivalence ratio can be found in the Supporting Information.

The uncertainty in ISW speed is determined according to the method presented in Ref. 3 from the uncertainty of the distance between the pressure transducers $u(\Delta x)$ and the uncertainty of the measured time interval between the passage of the ISW over two pressure transducers $u(\Delta t)$. The uncertainty $u(\Delta x)$ is given by the measurement uncertainty of the caliper used to measure the distances between the axially distributed pressure sensors and amounts to 0.10392 mm. The uncertainty $u(\Delta t)$ originates from the detection of the ISW at the pressure transducer positions along the shock tube axis. The times of the passage of the ISW over the sensors are obtained from the recorded pressure time histories of the axially distributed pressure sensors by detection of local maximum gradient. The advantage of this is that the determination of the times of the passage of the ISW over the pressure sensors is unaffected by deviations in the individual sensors' sensitivities, which have to be considered in other measurement setups similar to Ref. 3. The pressure sensor record exhibits a continuous (yet very steep) increase in pressure when the ISW passes it. The cause of the continuous rise of the pressure in the recorded pressure signals can be attributed to the noninfinitely small sensor surface and the sensors' rise time behavior. The uncertainty $u(\Delta t)$ is conservatively estimated to correspond to the length of this continuous increase in pressure of maximum 1 μs, as the exact time of the passage of the ISW over the sensor lies in this time interval. A second term is added to $u(\Delta t)$, which describes that the data acquisition card only records the pressure signals at finite sampling time intervals of 0.1 μs.

The uncertainty of IDT measurement of first and main ignition stage $u(\tau)$ is determined from the uncertainty in test temperature $u(T_5)$, test pressure $u(P_5)$, and composition $u(X_i)$ with the law of propagation of uncertainty,[64]

$$u(\tau) = \sqrt{\left(\frac{\partial \tau}{\partial T_5}\right)^2 u^2(T_5) + \left(\frac{\partial \tau}{\partial P_5}\right)^2 u^2(P_5) + \sum_{i=1}^{N}\left(\frac{\partial \tau}{\partial X_i}\right)^2 u^2(X_i)}. \tag{13}$$

The sensitivities ($\frac{\partial \tau}{\partial T_5}, \frac{\partial \tau}{\partial P_5}, \frac{\partial \tau}{\partial X_i}$) are obtained numerically with a central difference scheme and employing a chosen chemical–kinetic model, either for the first or main ignition stage. Hence, the quality of the uncertainty estimate for IDT depends on the prediction of the relation between IDT and input quantities by the chosen chemical–kinetic model. Because of the nonlinear dependency of the IDT on the test temperature, second-order terms may need to be considered in the formulation for IDT uncertainty in Equation (13). It was verified that second-order terms in the temperature are negligible compared to the other uncertainty components, as they amount to less than 3% of the total uncertainty.

An additional uncertainty component of 12.5 μs is added to IDT uncertainty, which accounts for the extraction of IDT from the measured time histories of pressure and chemiluminescence data, with respect to when counting of IDT ends and starts. This value results from the oscillation of the pressure sensor with a frequency between 20 and 40 kHz when the reflected shock passes it, which causes an uncertainty with respect to the beginning of IDT within the first quarter period of the oscillation. The worst case estimate of this uncertainty of 12.5 μs is assumed for all measurements of first and main stage IDT. Note that oscillation and other effects causing uncertainty with respect to beginning of IDT (such as finite pressure sensor surface) are superposed, which is why they are not considered as additional uncertainty components. The chemiluminescence signal at 407 nm is relatively weak adding an additional uncertainty of 10% to the extraction of the moment of first-stage ignition. Note that extraction uncertainty becomes only significant for very short IDTs of the order of the extraction uncertainty. Nevertheless, measuring IDTs in shock tubes of less than 50 μs is not recommended.[7]

The uncertainty of each measurement presented in this paper is analyzed in depth with the analysis presented above. The maximum uncertainties of species mole fractions in the prepared gas mixtures are 1.80% for DME, 1.46% for oxygen, and 1.01% for the diluent gas (average values: 1.1% for DME, 1.3% for oxygen, and 0.8% for the diluent gas). The maximum uncertainty in test temperature amounts to 24.8 K or 1.96%, and the maximum uncertainty in test pressure amounts to 0.66 bar or 3.8%. On average, the uncertainty when determining the test temperature amounts to 8.9 K (0.82%) and 0.24 bar (1.9%) for the test pressure. For estimating the sensitivity functions in Equation (13) the chemical–kinetic model AramcoMech 3.0 is chosen, as it shows good agreement with measurement data.[39] The resulting uncertainty in IDT is estimated to a maximum of 56.2% and 16.7% on average. Note that large uncertainty is present for short IDTs, which is caused by the relatively high extraction uncertainty component. When extraction uncertainty is not considered, a significantly lower maximum uncertainty of 28.8% is present in the measurement, while the average uncertainty is only slightly lower with 13.5%. This proves that only a small fraction of measured IDTs exhibits high uncertainty. At the same time, this demonstrates the importance of considering extraction uncertainty for very short IDTs.

5.2 | Analysis of uncertainty components

From the different uncertainty contributions to IDT uncertainty, the contribution from test temperature uncertainty is recognized by all researchers as significant (Table 3), as IDT is strongly dependent on test temperature. The ISW speed is mostly considered as an uncertainty cause for test temperature, while the influence of initial temperature and mixture composition uncertainty is often neglected (Table 3). In the following, the relative importance of the different uncertainty components regarding the test temperature will be analyzed. Based on that analysis, it will be discussed whether a neglection of a certain component may lead to underprediction of uncertainty depending on the test gas mixture. It should be emphasized that IDTs are often measured highly diluted in argon (Table 1), while this publication focuses on undiluted fuel–air mixtures.

Sensitivity functions (i.e., $\frac{\partial T_5}{\partial T_1}$, $\frac{\partial T_5}{\partial W_s}$, $\frac{\partial T_5}{\partial X_i}$ in Equation 11) determine the weight with which an input uncertainty contributes to the overall test temperature uncertainty. Hence, they are the base for assessing the susceptibility of the test temperature measurement to certain input quantities.

To analyze how the importance of uncertainty contributions for test temperature change between a DME–oxygen mixture highly diluted in argon and a DME–air mixture, the sensitivity functions of the stoichiometric mixtures M1 and M3 are compared. Significantly different sensitivity magnitudes are observed for mixtures M1 and M3 (Figure 9). In contrast, the sensitivity of the test temperature to all the input quantities exhibits merely a slight dependency on the equivalence ratio of the DME–air mixture (compare mixtures M2–M4 in Figure 9). The sensitivity of the test temperature to the ISW velocity dT_5/dW_s of mixture M1 is higher compared to M3, whereas the sensitivity to the initial temperature dT_5/dT_1 is lower for all considered test temperatures for mixture M1. Thus, the uncertainty in ISW velocity contributes to the combined uncertainty in the test temperature with a lower weight for the DME–air mixture, while the uncertainty in the initial temperature contributes with a higher weight compared to the DME–oxygen mixture highly diluted in argon. It is additionally to note that, for both mixtures M1 and M3, the test temperature shows the highest absolute sensitivity to the DME mole fraction (Figure 9, right) out of all species.

A comparison of the influence of different uncertainty components is complicated from analyzing sensitivity functions only, as the input quantities, as well as their uncertainties, exhibit different magnitudes. To account for this, the contribution of each input quantity is considered in the following as the absolute value of the product of sensitivity function and input uncertainty ($|\frac{\partial T_5}{\partial T_1} \cdot u(T_1)|$, $|\frac{\partial T_5}{\partial W_s} \cdot u(W_s)|$, $|\frac{\partial T_5}{\partial X_i} \cdot u(X_i)|$, compare Equation 11). Meaning, for each uncertainty source the resulting uncertainty in test temperature is determined. In the following, it is investigated with the help of these contributions whether it is always valid to determine the uncertainty in test temperature based on the uncertainty in ISW speed solely, as it is sometimes done in the literature (Table 3). In other words, it will be examined whether a neglection of the uncertainty contributions from composition and initial temperature will lead to an underprediction of test temperature uncertainty. In order to do this, a case of very low uncertainty in ISW speed (2.7 m/s) and high uncertainty in

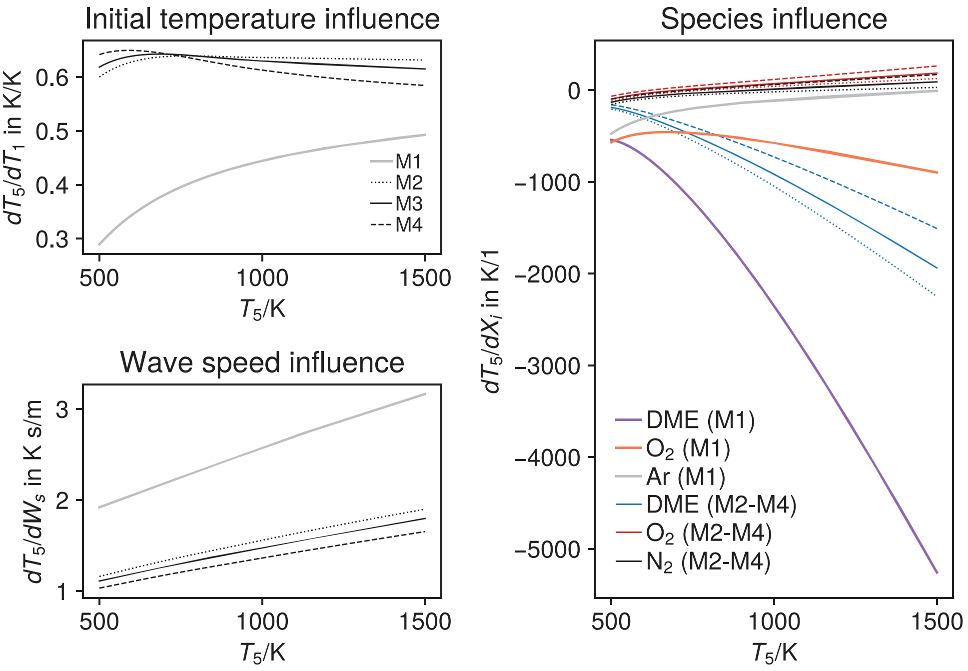

FIGURE 9 Sensitivity functions of test temperature for DME–synthetic air mixture at different equivalence ratios (M2–M4) and argon-diluted DME–oxygen mixture (M1) [Color figure can be viewed at wileyonlinelibrary.com]

FIGURE 10 Test temperature uncertainty contribution from ISW speed, composition, and initial temperature uncertainty compared to overall temperature uncertainty (statistical RSS and brute-force estimate). Two cases of different uncertainty in ISW speed of 2.7 and 5.4 m/s are considered [Color figure can be viewed at wileyonlinelibrary.com]

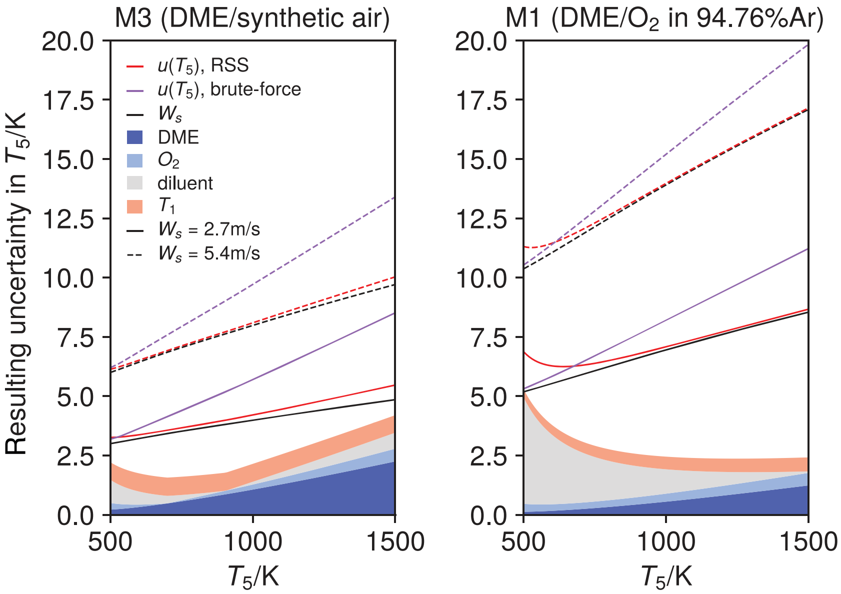

the other components ($u(T_1) = 1.2$ K, $u(X_{\mathrm{DME}}) = 1.8\%$, $u(X_{\mathrm{O_2}}) = 1.5\%$, $u(X_{\mathrm{Ar/N_2}}) = 1.0\%$) is analyzed for the stoichiometric mixtures M1 and M3. In Figure 10, all uncertainty components other than ISW speed are illustrated as a stacked area plot to compare their contribution with the contribution of ISW speed to test temperature uncertainty. Even for the presented case of very low uncertainty in ISW speed, the ISW speed is still the largest test temperature uncertainty source for both mixtures (Figure 10). However, the from ISW speed resulting uncertainty in test temperature is smaller by almost a factor of two for the DME–air mixture M3 (Figure 10), which can be attributed to the lower sensitivity $\partial T_5/\partial W_s$ of mixture M3 compared to M1 (Figure 9). Because of the lower uncertainty contribution from ISW speed, the sum of all other uncertainty contributions is comparably large for mixture M3 (compare shaded area to black solid line in Figure 10). However, the total uncertainty in test temperature is only marginally larger than the contribution from ISW speed for both mixtures, indicating that the other uncertainty components are not significant. For a case with larger uncertainty in ISW speed (dashed lines in Figure 10, factor of two), the difference is even smaller indicating an even smaller significance of components other than ISW speed for cases with a less extreme distribution of uncertainties. The reason for this is the calculation method of the overall uncertainty as root sum of squares of the components (RSS, compare Equation 11). Uncertainty components only become important when they are relatively large compared to the largest uncertainty component, in this case resulting from the ISW speed.

However, at high temperatures the deviation between the overall uncertainty in test temperature and contribution from ISW speed deviates slightly, indicating that other uncertainty contributions may be important. To further carefully examine the influence of uncertainty contributions, test temperature uncertainty is additionally estimated conservatively with a brute-force method. For each condition, the largest deviation in temperature is chosen from all possible combinations of variations in the inputs $T_1 \pm u(T_1)$, $X_i \pm u(X_i)$, $W_s \pm u(W_s)$. The test temperature uncertainty is conservatively assumed to equal this largest deviation. At high temperatures, the overall brute-force uncertainty in test temperature shows a large deviation to the uncertainty resulting from ISW speed solely (purple and black lines in Figure 10), indicating that uncertainty components apart from ISW speed have to be considered to accurately predict brute-force temperature uncertainty. However, the brute-force uncertainty estimate is based on the case of the worst possible combination of input uncertainties and is therefore very unlikely to occur.

To conclude, for the mixtures studied in this work the assumption to infer test temperature from ISW velocity uncertainty only leads to a very small underprediction of the standard statistical (RSS) test temperature uncertainty. However, if uncertainty is estimated very conservatively with a brute-force method other uncertainty components significantly contribute to overall test-temperature uncertainty, especially for the undiluted DME–air mixture.

Not only for the uncertainty in test temperature but also for the uncertainty in IDT, different calculation approaches are pursued in the literature. Uncertainty in IDT arises from its dependency on temperature, pressure, and mixture composition, besides uncertainties arising from IDT definition and extraction from measurement data. While the propagation of test temperature uncertainty into IDT uncertainty is considered in all of the analyzed publications (Table 3), uncertainty in test pressure and mixture composition is not always considered as IDT uncertainty cause. This again raises the question whether the neglection of uncertainty components leads to underprediction of IDT uncertainty. Therefore, it is investigated how significant different IDT uncertainty components are.

Sensitivity functions of IDT ($\frac{\partial \tau}{\partial T_5}$, $\frac{\partial \tau}{\partial P_5}$, $\frac{\partial \tau}{\partial X_i}$ in Equation 13) are used to analyze the weight of different uncertainty contributions for all investigated mixtures (Figures 11 and 12), similar to the analysis of test temperature uncertainty. The sensitivities presented here are estimated with AramcoMech 3.0.[67]

The sensitivity of IDT to test temperature $\partial\tau/\partial T_5$ exhibits zero crossings due to negative temperature coefficient (NTC) behavior of DME (Figure 11, top left). At values with $\partial\tau/\partial T_5$ close to zero, the uncertainty in test temperature contributes only little to IDT uncertainty. At the same time, the sensitivity functions of IDT to pressure $\partial\tau/\partial P_5$ and mixture composition $\partial\tau/\partial X_i$ (Figure 11, top right and bottom) exhibit extrema in the intermediate temperature range (Figure 11, top right and bottom). Hence, uncertainties in test pressure and mixture composition will contribute with a higher weight to overall IDT uncertainty in this temperature range, which indicates that they may be important for accurate determination of overall IDT uncertainty. The extrema in $\partial\tau/\partial P_5$ and $\partial\tau/\partial X_i$ are shifted to higher temperatures at higher test pressures and larger equivalence ratios.

All of the sensitivity functions exhibit larger absolute values at low pressures and equivalence ratios (Figure 11 and 12). Furthermore, the magnitude of sensitivity functions is significantly higher for the argon-diluted mixture M1 (compare Figure 11 and 12).

However, it is again difficult to conclude the significance of input uncertainty from sensitivity functions solely, as uncertainties in the input quantities also exhibit different magnitudes. Analogous to the analysis of test temperature uncertainty, example values of input uncertainties are used to determine their resulting contribution to IDT uncertainty ($|\frac{\partial \tau}{\partial T_5} \cdot u(T_5)|$, $|\frac{\partial \tau}{\partial P_5} \cdot u(P_5)|$, $|\frac{\partial \tau}{\partial X_i} \cdot u(X_i)|$, compare Equation 13). Here, average values from the measurements conducted in the scope of this publication are chosen for the input uncertainties of 0.82% in T_5, 1.9% in P_5, 1.1% in X_{DME}, 1.3 % in $X_{\mathrm{O_2}}$, and 0.8% in $X_{\mathrm{N_2/Ar}}$. Again, all uncertainty components other than temperature are presented as a stacked graph to compare their contribution to IDT uncertainty with the contribution from temperature (Figure 13). In order to investigate the influence of mixture composition on the magnitudes of different uncertainty components, both stoichiometric mixtures M3 and M1 are exemplary compared at 35 bar. The graphs for all other mixtures and pressures are provided in the Supporting Information (Figures 2 and 3). Especially in the intermediate test temperature region, the uncertainty contributions of pressure and composition to IDT uncertainty are relatively large compared to the uncertainty resulting from test temperature, as already indicated by analysis of sensitivity functions (Figure 13). In the intermediate tem-

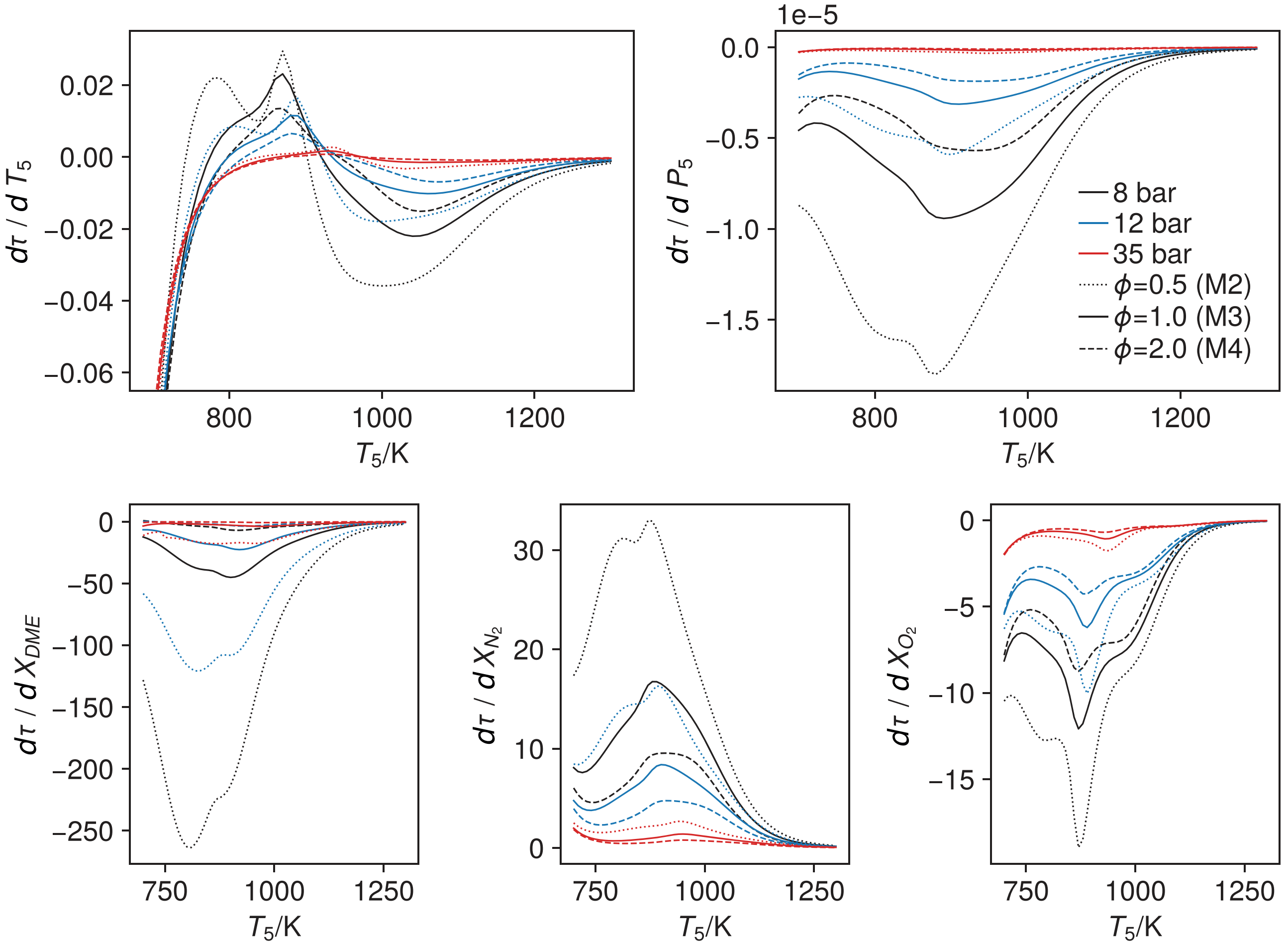

FIGURE 11 Sensitivity of IDT to test temperature, pressure, and mole fractions for DME–synthetic air mixtures at different equivalence ratios (mixtures M2–M4) and pressures [Color figure can be viewed at wileyonlinelibrary.com]

perature range, the overall RSS uncertainty of IDT differs significantly from IDT uncertainty caused by test temperature only, demonstrating that other uncertainty contributions substantially add to overall IDT uncertainty. That means, neglecting the uncertainty in IDT, which is caused by uncertainty of test pressure and species mole fraction, would underestimate the uncertainty of IDT in the intermediate temperature range.

The magnitude of the different uncertainty components only shows a weak dependency on test pressure and stoichiometry, while the region with significant contribution from pressure and composition is shifted to higher temperatures for larger equivalence ratios and higher pressures (compare Figures 2 and 3 in the Supporting Information).

The small resulting uncertainty from test temperature in the intermediate temperature range can be attributed to NTC behavior. This indicates that for fuels with NTC behavior a neglection of uncertainty components other than test temperature may lead to a significant underprediction of IDT uncertainty in the intermediate temperature range. Whereas for fuels that do not exhibit NTC behavior approximating IDT uncertainty by solely considering test temperature as an uncertainty source may not lead to underprediction. However, careful analysis from case to case is necessary.

Note that the uncertainties in test pressure and test temperature which propagate into IDT uncertainty originate from uncertainties in species mole fraction, initial temperature and pressure, and ISW velocity. Hence, it is possible to distinguish species mole fraction, initial temperature and pressure, and ISW velocity as uncertainty contributors of IDT uncertainty (Figures 4 and 5 in the Supporting Information).

6 | IDT MEASUREMENT OF DME

IDTs of DME are measured highly diluted in argon (mixture M1) at a mean pressure of 10.4 bar aiming at validating the measurement method. Furthermore, a series of undiluted IDT measurements of DME–air mixtures at lean, stoichiometric, and rich conditions is performed

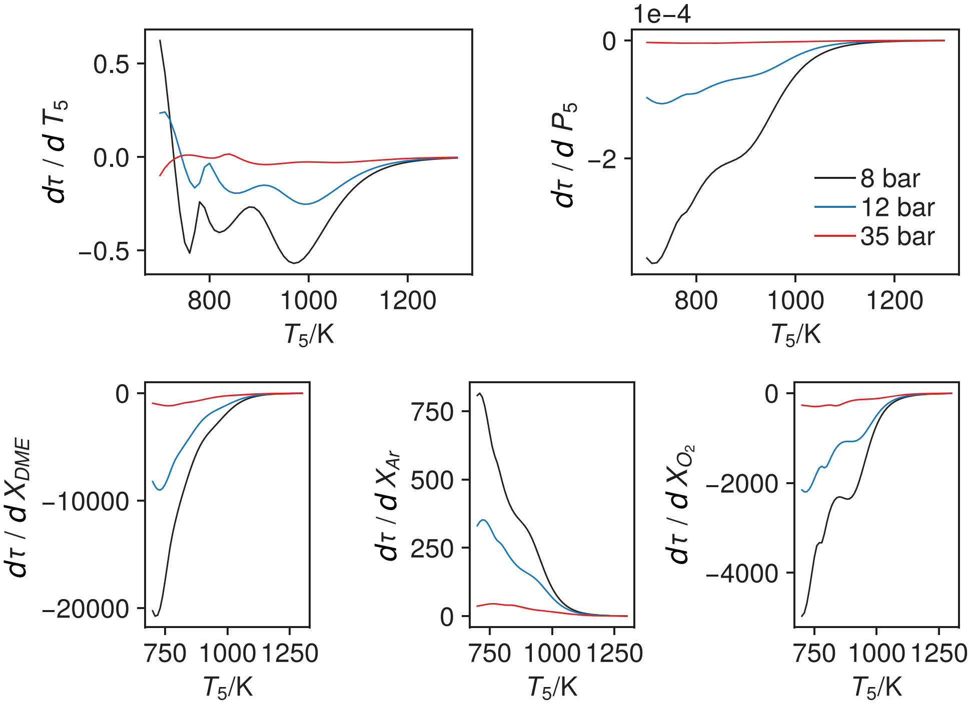

FIGURE 12 Sensitivity of IDT to test temperature, pressure, and mole fractions for highly in argon-diluted mixture M1 at different pressures [Color figure can be viewed at wileyonlinelibrary.com]

FIGURE 13 Relative uncertainty in IDT caused by uncertainties in test temperature, composition, and test pressure for stoichiometric DME–synthetic air mixture (M3) and stoichiometric argon-diluted DME/oxygen mixture (M1) at 35 bar [Color figure can be viewed at wileyonlinelibrary.com]

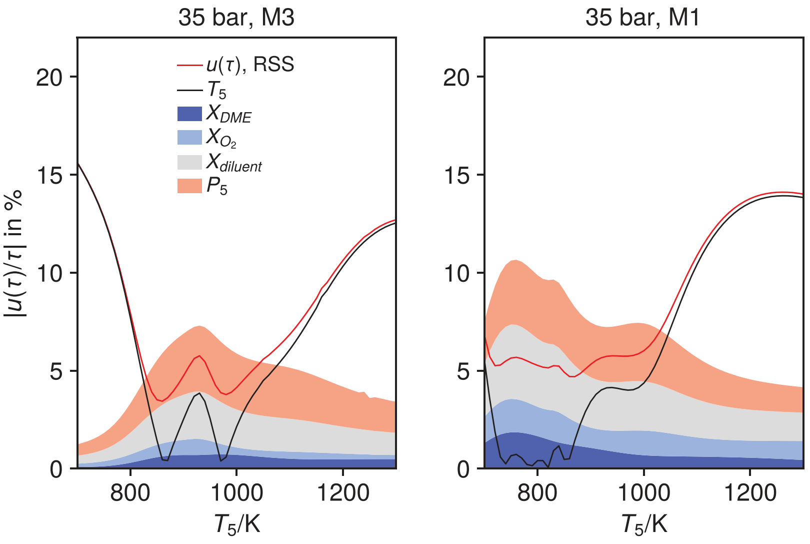

at the mean pressures listed in Table 4.[1] Note that for each measurement point, the measurement conditions are achieved behind a reflected shock wave, that is they cannot be set directly. Therefore, the measurement pressure varies slightly from measurement point to point and thus a mean pressure is provided. The exact measurement conditions for each measurement point together with their IDTs are provided in the Supporting Information (Tables 1–4). Furthermore, DME is known to exhibit NTC behavior and two-stage ignition. For the measurements at approximately 35 bar, first-stage IDT is also detected as described in Section 2.

TABLE 4 Average pressures of undiluted measurements

ϕ	Mean pressure (bar)		
0.5	7.6	11.6	34.9
1.0	7.8	12.9	34.9
2.0	7.6	11.3	35.4

---

[1] IDT data at equivalence ratio of 1 and pressure of approximately 35 bar is already published in Ref. 39.

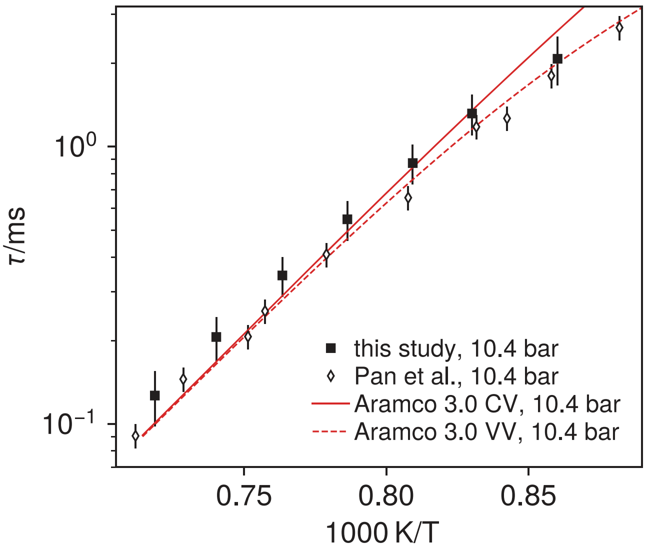

FIGURE 14 Measured IDT for mixture M1 in comparison to data from Pan et al.[21] Model prediction with Aramco-Mech 2.0 with constant volume (CV) assumption and accounting for nonideal pressure increase of 4%/ms (VV) [Color figure can be viewed at wileyonlinelibrary.com]

6.1 | Validation of method

In order to validate the measurement method in the newly built facility, IDTs are measured and compared to corresponding literature data for both, DME–air mixtures and highly in argon-diluted mixtures , and to predictions by the recent detailed chemical–kinetic model AramcoMech 3.0.[67]

Figure 14 compares measured IDTs of mixture M1 to data from Pan et al.[21] Both data agree very well within their corresponding measurement uncertainty, indicating that the measurement method in the newly built shock tube is applicable for highly diluted mixtures. Note that IDT uncertainties in Ref. 21 are determined based on temperature uncertainty, which is determined from the uncertainty in ISW speed, solely. The present uncertainty analysis includes additional uncertainty sources.

Validation measurements with undiluted DME–air mixtures are performed at a mean pressure of approximately 12 bar at equivalence ratios of 0.5, 1.0, and 2.0 (Figure 15). al.[29] observed at an equivalence ratio of 1 in the NTC temperature range can be explained by the deviation in test pressure between the two data sets. IDTs in Ref. 29 are measured at a lower pressure than the data presented here, which is recorded at around 13 bar in the NTC-temperature range. IDTs are in better agreement with the ones reported in Ref. 28.

6.2 | IDTs of undiluted DME–air mixtures

In order to investigate the influence of pressure and equivalence ratio on IDTs of DME–air mixtures over a range of temperatures, measurements are conducted at mean pressures of approximately 8, 12, and 35 bar and at equivalence ratios of 0.5, 1.0, and 2.0 (see Table 4). Additionally, constant volume and variable volume simulations are performed at the average pressure of each measurement curve. As described in Section 3, the nonideal pressure rise is integrated into variable volume modeling based on the correlation to the actual measured nonideal pressure rise (Equation 4). That means, a specific nonideal pressure rise is used for each condition and mixture. This approach circumvents using the same nonideal pressure rise over a range of conditions, as commonly done in the literature, for example, in Refs. 18, 21, 22, 24, 26.

Figure 16 compares the prediction of IDTs for the most recently developed chemical–kinetic model AramcoMech 3.0 to the measurement data using both modeling assumptions, constant, and variable volume. Additionally, the comparison to measurement data has been conducted with other detailed chemical–kinetic models and is provided in the Supporting Information (Figures 6–8). DME–air mixtures exhibit a NTC region (Figure 16), which is also observed in other studies, for example, Refs. 28 and 29. As expected, a pressure increase from 8 to 35 bar decreases IDTs significantly over the whole temperature range (Figure 16). The temperature region with NTC behavior is shifted to higher temperatures when the pressure is increased (Figure 16, $\phi = 1.0$, and $\phi = 2.0$), which is also observed in other studies, for example, Refs. 28 and 29. With increasing equivalence ratio, IDTs of DME–air mixtures decrease (Figure 17) and the NTC temperature region is shifted to higher temperatures.[29]

The difference between constant and variable volume modeling is especially significant at low temperatures and pressures, as long IDTs are more affected by the nonideal pressure increase behind the reflected shock[6] (Figure 16). However, due to the slight pressure variation between measurement points, it is not possible to assess which modeling approach represents the data better solely based on Figure 16. Therefore, this will be investigated in the next section from simulations that resemble the conditions in each measurement point.

First-stage IDT is investigated at a pressure of approximately 35 bar for all investigated equivalence ratios. Measured IDTs of the first and main ignition stages are compared to the prediction of AramcoMech 3.0 at the mean pressure provided in Table 4 (Figure 17). First-stage ignition is not very sensitive to the equivalence ratio (Figure 17). This was already observed for *n*-heptane[42] and for

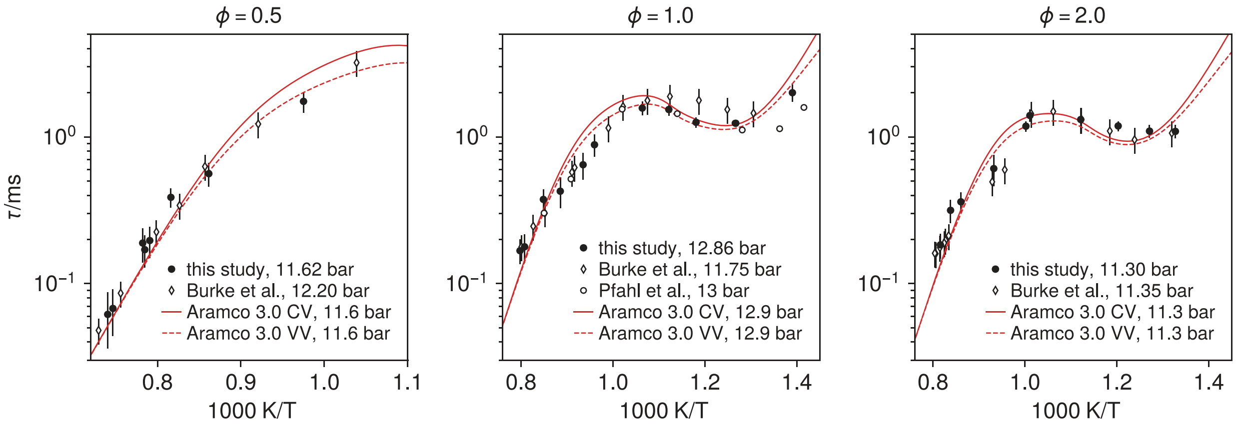

FIGURE 15 Measured IDTs for mixtures M2, M3, and M4 in comparison to data from Burke et al.[29] and Pfahl et al.[28] Model prediction with Aramco-Mech 2.0 with constant volume (CV) assumption and accounting for non-ideal pressure rise obtained with correlation (4) (VV) [Color figure can be viewed at wileyonlinelibrary.com]

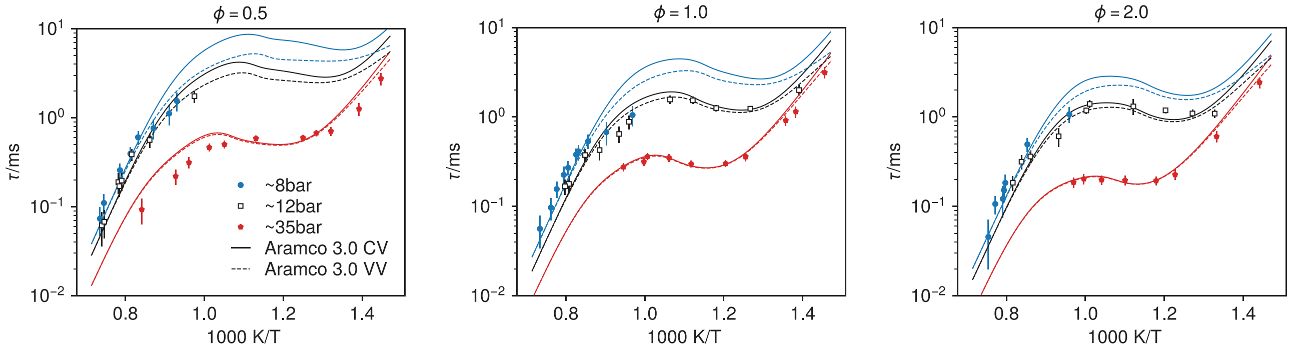

FIGURE 16 Temperature dependency of IDT of DME–air mixtures at pressures of approximately 8, 12, and 35 bar and equivalence ratios ϕ of 0.5, 1.0, and 2.0. Comparison to prediction by Aramco Mech 3.0 using constant (CV) and variable (VV) volume modeling [Color figure can be viewed at wileyonlinelibrary.com]

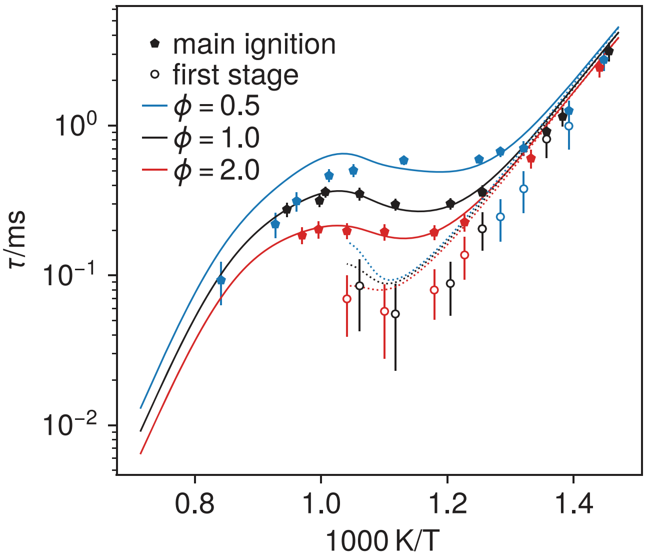

FIGURE 17 Temperature dependency of first-stage IDT of DME–air mixtures of different equivalence ratios at 35 bar. Comparison to variable volume model prediction with AramcoMech 3.0 [Color figure can be viewed at wileyonlinelibrary.com]

CO_2-diluted DME–air mixtures.[39] Mittal et al.[25] report a weak dependency on oxygen mole fraction, which is not observed here, as the oxygen mole fraction varies less compared to the mixtures investigated in Ref. 25. The slight deviation between the prediction by Aramco Mech 3.0 and the experimentally recorded first-stage IDT may be attributed to the difficult measurement yielding a weak signal and a correspondingly a high signal-to-noise ratio. However, the general tendency is reproduced very well by AramcoMech 3.0.

6.3 | Prediction by chemical mechanisms

With the measured IDTs, it is assessed how well available chemical–kinetic models predict IDTs of undiluted DME–air mixtures. Based on topicality and comprehensiveness, seven models for DME ignition are chosen for comparison to measurement data. The chemical–kinetic models, together with the validation data for IDTs which was used upon publication of the respective model, are

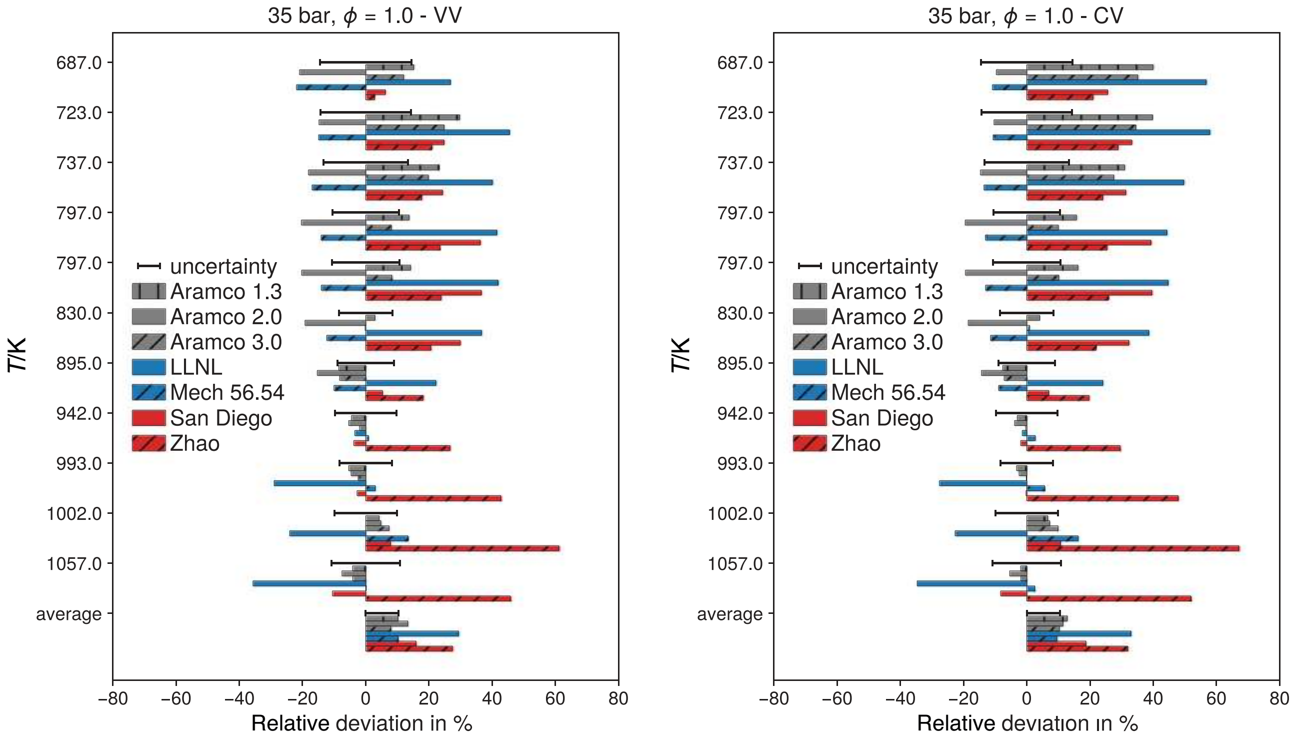

FIGURE 18 Deviation between kinetic model prediction and measured IDT with variable volume (VV, left) and constant volume assumption (CV, right) at 35 bar and for stoichiometric mixture M3. Measurement uncertainties are provided as error bars [Color figure can be viewed at wileyonlinelibrary.com]

listed in Table 5. Note that, for AramcoMech 3.0, it is assumed that the same validation data as NUIG Mech 56.54 were used, as it builds on it.[67] IDTs of undiluted DME–air mixtures are used as validation data as reported by Pfahl et al.,[28] Burke et al.,[29] Li et al.,[26] and from Mittal et al.[25] Recently published chemical–kinetic models for DME use more measurement data of undiluted mixtures for validation, as it was available upon model construction, whereas LLNL DME Mech and Princeton Zhao Mech only use data of undiluted mixtures from Pfahl et al.[28]

In order to compare measurement and model prediction, simulations are conducted that resemble the conditions in each measurement point (as provided in Supporting Information Tables 1–4) to determine which mechanisms reproduces the measurement data best. Constant, as well as variable volume simulations, with the nonideal pressure rise taken from the correlation (4) are conducted. The relative deviation between modeled IDT τ_{mech} and measured IDT τ_{meas} is determined as

$$\frac{\tau_{\text{mech}}(T,P,\phi)-\tau_{\text{meas}}(T,P,\phi)}{\tau_{\text{meas}}(T,P,\phi)}. \tag{14}$$

Figure 18 shows the relative deviation between measurement points and model prediction of IDT exemplary for stoichiometric composition at 35 bar. Additionally, in Figure 18 an average of the relative deviation between measured and modeled IDT over the investigated temperature range $(T_N - T_0)$ is provided,

$$\frac{1}{T_N - T_0}\int_{T_0}^{T_N}\left|\frac{\tau_{\text{mech}}(T,P,\phi)-\tau_{\text{meas}}(T,P,\phi)}{\tau_{\text{meas}}(T,P,\phi)}\right| dT. \tag{15}$$

The integral in (15) is approximated at the measurement points using the trapezoidal rule.

For most temperatures and chemical–kinetic models, variable volume modeling shows less deviation to measurement data (Figure 18). The models from the AramcoMech family generally exhibit good agreement with the measurement data. For most temperatures, the deviation between mechanism prediction and measured IDT is within measurement uncertainty. AramcoMech 3.0 shows the best agreement to measurement data of all the considered models (Figure 18). The due to its small number of species widely used Princeton Zhao Mech shows good agreement to the measurement data at low temperatures . However, Princeton Zhao Mech overpredicts IDTs at intermediate temperatures significantly, owing to a shift of predicted IDTs to higher values and a too high steepness of the IDT's temperature dependency in the NTC-region com-

TABLE 5 Chemical–kinetic models for DME

		Validation: IDT of mixtures with pure DME				
Name	**Reference(s)**	**Mixture**	ϕ	P**(bar)**	T **(K)**	**Reference**
LLNL DME Mech	68–70	1%DME/O_2/Ar	0.5, 1, 2	3.5	1200–1600	12
		DME/synthetic air	1	13, 40	650–1300	28
Princeton Zhao Mech	71	DME/synthetic air	1	13, 40	650–1300	28
		1%DME in O_2/Ar	0.5, 1, 2	3.5	1200-1600	12
		1%DME in O_2/Ar	1, 2	1.82	1250–1540	13
NUIG Mech 56.54, AramcoMech 3.0	29, 67	2.86%DME in O_2/N2	0.43, 0.75, 1.5	10,15,20	615–735	25
		DME/synthetic air	1	13, 40	650–1300	28
		1%DME in O_2/Ar	0.5, 1.0, 2.0	1.6-6.6	1175–1480	14
		1.309% DME in O_2/Ar	1.0	1, 5, 10	1165–1576	15
		DME/synthetic air	0.3, 0.5, 1.0, 2.0	7-10, 11, 25, 30	651–1428	29
		1.25%DME in O_2/Ar	0.5, 1.0, 2.0	1.9	1261–1700	72
		DME/synthetic air, 0/20/40% N2	0.5, 1.0, 1.5;	22-23	697–1239	26
San Diego DME Mech	73	DME/synthetic air	1	13, 40	650–1300	28
		1%DME in O_2/Ar	1, 2	1.82	125–1540	13
		DME/synthetic air	0.5, 1.0, 2.0	7-10, 11, 25, 30	651-1428	29
		1.31%DME in O_2/Ar	1	20	1170–1416	74
Aramco Mech 1.3	75	DME/synthetic air	0.3, 0.5, 1.0, 2.0	2, 11, 25	651–1428	29
		1%DME in O_2/Ar	0.5, 1.0, 2.0	3.3	1190–1470	14
AramcoMech 2.0	76-81	1%DME in O_2/Ar	0.5, 1.0, 2.0	3.3	1190–1470	14
		DME/synthetic air	0.3, 0.5, 1.0, 2.0	2, 11, 25	651–1428	29
		1.25%DME in O_2/Ar, 2.5%DME in O_2/Ar	0.5, 1.0, 2.0, 2.0	1.9, 3.7	1261–1700	72

TABLE 6 Average deviation over the range of considered temperatures (determined with Equation 15) between measured and modeled IDTs (variable volume modeling) in percentage

Pressure	8			12			35		
ϕ	0.5	1.0	2.0	0.5	1.0	2.0	0.5	1.0	2.0
Mechanism									
LLNL DME Mech	20.84	21.27	16.64	10.11	14.40	19.58	35.12	29.29	30.43
Princeton Zhao Mech	19.07	32.91	36.69	19.20	28.22	23.38	63.18	27.39	29.59
NUIG Mech 56.54	25.50	34.26	32.11	17.47	19.62	22.23	36.89	10.22	13.21
San Diego DME Mech	41.32	36.74	41.25	41.41	18.41	16.71	24.43	15.87	19.82
AramcoMech 1.3	22.64	32.11	25.71	16.48	20.69	17.24	43.84	10.17	11.20
AramcoMech 2.0	25.45	34.31	32.86	20.21	20.64	24.28	32.74	13.31	14.52
AramcoMech 3.0	25.41	34.13	30.87	16.78	19.26	19.08	36.18	7.91	8.81

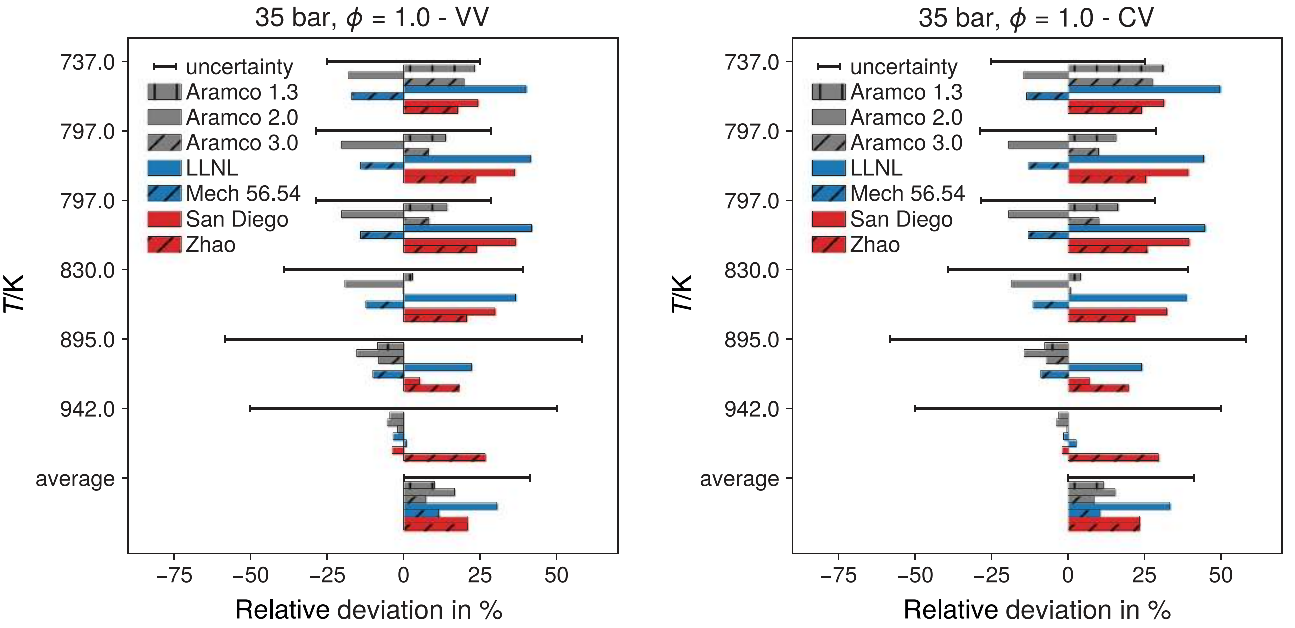

FIGURE 19 Deviation between kinetic model prediction and measured first-stage IDT with variable volume (VV, left) and constant volume assumption (CV, right) at 35 bar and for stoichiometric mixture. Measurement uncertainties are provided as error bars [Color figure can be viewed at wileyonlinelibrary.com]

pared to measured IDTs (see Figure 8 in Supporting Information).

For all the other investigated equivalence ratios and pressures, the comparison of measurement and model prediction similar to Figure 18 can be found in the Supporting Information (Figures 9 and 10). In order to briefly compare with model prediction over the whole range of pressures and equivalence ratios, the average deviation (compare Equation 15) is provided in Table 6. The prediction of IDTs from models of the AramcoMech family and NUIG Mech 56.54 is generally good. AramcoMech 3.0 shows very close agreement to measured IDTs for stoichiometric and rich mixtures at 35 bar.

Note that at 35 bar the lean mixture's IDT shows larger deviation to the prediction by all models, indicating a nonideal effect is present in the measurement at these conditions. In other studies, preignition in hotspots away from the end wall has been observed[82–84] caused by nonuniformities due to the interaction of the reflected shock with the boundary layer. These local ignition kernels induce pressure waves that travel to the measurement plane and decrease IDT at the end wall. Based on the available data, it is not possible to unambiguously confirm that local ignition kernels are the cause for the deviation between modeling and measurement. For further investigation, a measurement setup is needed with optical access, as, for example, in Ref. 85.

The model prediction of first-stage IDT is also compared to measurement data for a pressure of 35 bar exemplary for the stoichiometric mixture (Figure 19). Note that first-stage IDT is determined based on different time series in modeling and measurement data processing (Section 3). It is assumed that this only adds a negligible uncertainty compared to measurement uncertainty when comparing measured and modeled first-stage IDTs. AramcoMech 3.0 shows the closest agreement to measured first-stage IDT from all investigated mechanisms, while LLNL DME Mech as well as San Diego DME Mech tend to overpredict first-stage IDTs. It is important to emphasize that the measurement uncertainty is relatively large, and therefore a large fraction of model prediction is within measurement uncertainty.

The deviation between model prediction and measured first-stage IDTs similar to Figure 19 is provided in the Supporting Information for lean and rich mixtures (Figure 11). Generally, the chemical–kinetic models from the AramcoMech family and NUIG Mech 56.64 predict first-stage IDTs well for all investigated mixtures.

7 | CONCLUSION

A new shock tube facility for measurement of IDTs is introduced facilitating investigations of alternative synthetic fuels at practically relevant conditions. Due to their wide practical application, undiluted fuel–air mixtures are investigated in this publication, in contrast to highly argon-diluted fuel–oxygen mixtures which are often considered. This puts the focus on challenges related to shock tube measurements, as the nonideal pressure rise is larger for mixtures that are not highly diluted in argon.[5] Furthermore, undiluted fuel–air mixtures may engender additional significant components in uncertainty analysis of IDT measurement, which may have been previously neglected.

A series of nonreactive measurements in synthetic air and argon are performed to characterize shock tube behavior. First, the nonideal pressure rise is obtained from measurement data. Comparison to literature data shows similar shock tube performance as in Ref. 46 even though the internal diameter is smaller, indicating that the diameter effect on the nonideal pressure rise becomes less important for larger shock tube diameters. In order to integrate the nonideal pressure rise automated into chemical–kinetic modeling of fuel–air mixtures, a new approach is developed, which is based on measurement data of synthetic air. The advantage of this approach is that for each investigated condition and mixture a single nonideal pressure rise can be determined with minimal effort.

Furthermore, available test times are extracted for synthetic air and argon test gases from nonreactive measurement data. The experimentally determined test times differ from the prediction based on ideal shock tube behavior. A semiempirical model for test times is developed, which corrects the ideal shock tube test time calculation with nonreactive measurement data. The model shows very good agreement to measured test times of DME–air mixtures. With this model, test times of reactive mixtures can be determined easily from test time measurements of nonreactive mixtures without a complex model describing nonideal shock tube behavior. Thus, it is possible to predict available test times a priori and support the measurement by providing limits for experimental IDT.

A comprehensive uncertainty analysis is performed for the new shock tube facility to give very precise estimates of the measurement uncertainty. A literature review showed that uncertainty determination in shock tube IDT measurements is not handled universally. Therefore, a theoretical analysis on the significance of certain uncertainty contributions is performed. Test temperature uncertainty is often determined based on uncertainty in ISW velocity, while other possible uncertainty sources, such as mixture composition and initial temperature, are neglected. Analysis shows that this approach does not lead to a significant underprediction of test temperature uncertainty when the standard statistical calculation method is used. However, if test temperature uncertainty is determined conservatively with a brute-force method, additional uncertainty components have to be considered besides ISW speed uncertainty, especially for undiluted fuel–air mixtures. Nonetheless, brute-force uncertainty is based on a case with a very specific uncertainty distribution, which is very unlikely to occur. Therefore, if uncertainty in test temperature is to be determined with standard confidence, the ISW velocity can be assumed as the only uncertainty source without large underprediction of total test temperature uncertainty. Additionally, uncertainty sources of IDT are investigated for the studied reactive mixtures. In the literature, IDT uncertainty is often determined from uncertainty in test temperature solely. Analysis shows that test pressure and mixture composition are significant uncertainty sources in the intermediate temperature range, which can be attributed to DME's NTC behavior. Hence, for fuels with NTC behavior a comprehensive uncertainty analysis taking into account multiple uncertainty sources for IDT is recommended to accurately predict measurement uncertainty.

Reactive experiments are performed to validate the measurement method by comparison to literature data and to investigate the effect of pressure and equivalence ratio on IDT of DME–air mixtures. IDTs of DME–air mixtures decrease with increasing pressure and equivalence ratio in the investigated temperature range and NTC behavior is observed. Additionally, first-stage IDTs are reported for lean, stoichiometric, and rich DME–air mixtures at a pressure of 35 bar in order to extend the experimental data base of DME first-stage ignition, which is to this date still relatively scarce. It was found that first stage IDT is not very sensitive to the equivalence ratio of the mixture.

IDTs at the exact measurement conditions are computed with various chemical–kinetic models. Simulations that take into account nonideal shock tube behavior show closer agreement to measurement data. Generally, the prediction of measured IDTs by mechanisms from the AramcoMech family is very good.

Thus, the presented new approaches of integrating the nonideal pressure rise into modeling and the comprehensive uncertainty analysis support the interpretation and comparison of measurement data to model prediction and hence the evaluation of the reliability of chemical–kinetic models. In this way, they also support the development and validation of chemical–kinetic models in general.

DATA AVAILABILITY STATEMENT

The data that supports the findings of this study are available in the Supporting Information of this article. Raw measurement data of this study are available from the corresponding author upon reasonable request.

ACKNOWLEDGMENTS

The authors gratefully acknowledge funding by the Deutsche Forschungsgemeinschaft (DFG, German Research Foundation) as part of collaborative research center SFB 1029 “Substantial efficiency increase in gas turbines through direct use of coupled unsteady combustion and flow dynamics” (Project-ID 200291049) in project A08. Additionally, they would like to thank the Chair of Fluid Dynamic at TU Berlin and Prof. Dr. Christian Oliver Paschereit. Thanks for technical support goes to Dr. Sebastian Schimek, Thorsten Dessin, and Andy Göhrs. For the electrical and LabVIEW support, the authors thank Heiko Stolpe, Christian Menzel, Martin Franke, David Holst, Marvin Schönlau, and Udo Schwadtke. Furthermore, they thank Iwo Gotthans, Christoph Peisdersky and Mike Rekus for their support in experiments.

Open access funding enabled and organized by Projekt DEAL.

REFERENCES

1. Braun-Unkhoff M, Goos E, Kathrotia T, et al. The importance of detailed chemical mechanisms in gas turbine combustion simulations. *Eurasian Chem Technol J*. 2014;16(2-3):179.
2. Law CK, Wu F, Egolfopoulos FN, Gururajan V, Wang H. On the rational interpretation of data on laminar flame speeds and ignition delay times. *Combust Sci Technol*. 2015;187(1-2):27–36.
3. Petersen EL, Rickard MJA, Crofton MW, Abbey ED, Traum MJ, Kalitan DM. A facility for gas- and condensed-phase measurements behind shock waves. *Meas Sci Technol*. 2005;16(9):1716–1729.
4. Bhaskaran KA, Roth P. The shock tube as wave reactor for kinetic studies and material systems. *Prog Energy Combust Sci*. 2002;28(2):151–192.
5. Hargis J, Petersen EL. Shock-tube boundary-layer growth effects on reflected-shock conditions in bath gases with and without CO_2. In *55th AIAA Aerospace Sciences Meeting*. American Institute of Aeronautics and Astronautics; 2017.
6. Petersen EL, Hanson RK. Nonideal effects behind reflected shock waves in a high-pressure shock tube. *Shock Waves*. 2001;10:405–420.
7. Davidson DF, Hanson RK. Interpreting shock tube ignition data. *Int J Chem Kinet*. 2004;36(9):510–523.
8. Chaos M, Dryer FL. Chemical-kinetic modeling of ignition delay: considerations in interpreting shock tube data. *Int J Chem Kinet*. 2010;42(3):143–150.
9. Nativel D, Cooper SP, Lipkowicz T, Fikri M, Petersen EL, Schulz C. Impact of shock-tube facility-dependent effects on incident- and reflected-shock conditions over a wide range of pressures and Mach numbers. *Combust Flame*. 2020;217:200–211.
10. Li H, Owens ZC, Davidson DF, Hanson RK. A simple reactive gasdynamic model for the computation of gas temperature and species concentrations behind reflected shock waves. *Int J Chem Kinet*. 2008;40(4):189–198.
11. Reaction Design. *SENKIN: A Program for Predicting Homogeneous Gas Phase Chemical Kinetics in a Closed System with Sensitivity Analysis*. Technical report, SEN-036-1, CHEMKIN Collection Release 3.6; 2000.
12. Dagaut P, Daly C, Simmie JM, Cathonnet M. The oxidation and ignition of dimethyl ether from low to high temperature (500–1600 K): experiments and kinetic modeling. In *Symposium (International) on Combustion*, Vol. 27. Amsterdam: Elsevier; 1998:361–369.
13. Bowman CT, Golden DM, Hanson RK, et al. *Optimization of Synthetic Oxygenated Fuels for Diesel Engines Investigators*. Technical Report, GCEP Technical Report; 2006.
14. Cook RD, Davidson DF, Hanson RK. Shock tube measurements of ignition delay times and OH time-histories in dimethyl ether oxidation. *Proc Combust Inst*. 2009;32(1):189–196.
15. Tang C, Wei L, Zhang J, Man X, Huang Z. Shock tube measurements and kinetic investigation on the ignition delay times of methane/dimethyl ether mixtures. *Energy Fuels*. 2012;26(11):6720–6728.
16. Hu E, Jiang X, Huang Z, Zhang J, Zhang Z, Man X. Experimental and kinetic studies on ignition delay times of dimethyl ether/*n*-butane/O_2/Ar mixtures. *Energy Fuels*. 2012;27(1):530–536.
17. Hu E, Zhang Z, Pan L, Zhang J, Huang Z. Experimental and modeling study on ignition delay times of dimethyl ether/propane/oxygen/argon mixtures at 20 bar. *Energy Fuels*. 2013;27(7):4007–4013.
18. Jiang X, Zhang Y, Man X, Pan L, Huang Z. Shock tube measurements and kinetic study on ignition delay times of lean DME/*n*-butane blends at elevated pressures. *Energy Fuels*. 2013;27(10):6238–6246.
19. Pan L, Hu E, Zhang J, Zhang Z, Huang Z. Experimental and kinetic study on ignition delay times of DME/H_2/O_2/Ar mixtures. *Combust Flame*. 2014;161(3):735–747.Special Issue on Alternative Fuels.
20. Geng Z, Xu L, Li H, Wang J, Huang Z, Lu X. Shock tube measurements and modeling study on the ignition delay times of *n*-

butanol/dimethyl ether mixtures. *Energy Fuels*. 2014;28(6):4206–4215.

21. Pan L, Hu E, Deng F, Zhang Z, Huang Z. Effect of pressure and equivalence ratio on the ignition characteristics of dimethyl ether-hydrogen mixtures. *Int J Hydrogen Energy*. 2014;39(33):19212–19223.
22. Pan L, Hu E, Tian Z, Yang F, Huang Z. Experimental and kinetic study on ignition delay times of dimethyl ether at high temperatures. *Energy Fuels*. 2015;29(5):3495–3506.
23. Ye W, Shi JC, Zhang RT, et al. Experimental and kinetic modeling study of CH_3OCH_3 ignition sensitized by NO_2. *Energy Fuels*. 2016;30(12):10900–10908.
24. Jiang X, Deng F, Yang F, Huang Z. Ignition delay characteristics and kinetic investigation of dimethyl ether/ *n* -pentane binary mixtures: interpreting the effect of the equivalence ratio and dimethyl ether blending. *Energy Fuels*. 2018;32(3):3814–3823.
25. Mittal G, Chaos M, Sung C-J, Dryer FL. Dimethyl ether autoignition in a rapid compression machine: experiments and chemical kinetic modeling. *Fuel Process Technol*. 2008;89(12):1244–1254.
26. Li Z, Wang W, Huang Z, Oehlschlaeger MA. Dimethyl ether autoignition at engine-relevant conditions. *Energy Fuels*. 2013;27(5):2811–2817.
27. Djordjevic N, Rekus M, Vinkeloe J, Zander L. Shock tube and kinetic study on the effects of CO_2 on dimethyl ether autoignition at high pressures. *Energy Fuels*. 2019;33(10):10197–10208.
28. Pfahl U, Fieweger K, Adomeit G. Self-ignition of diesel-relevant hydrocarbon-air mixtures under engine conditions. *Symposium (International) on Combustion*. 1996;26(1):781-789.
29. Burke U, Somers KPO'Toole P, et al. An ignition delay and kinetic modeling study of methane, dimethyl ether, and their mixtures at high pressures. *Combust Flame*. 2015;162(2):315–330.
30. Dames EE, Rosen AS, Weber BW, Gao CW, Sung C-J, Green WH. A detailed combined experimental and theoretical study on dimethyl ether/propane blended oxidation. *Combust Flame*. 2016;168:310–330.
31. Jiang X, Tian Z, Zhang Y, Huang Z. Shock tube measurement and simulation of DME/n-butane/air mixtures: effect of blending in the NTC region. *Fuel*. 2017;203:316–329.
32. Shi Z, Zhang H, Wu H, Xu Y. Ignition properties of lean DME/H_2 mixtures at low temperatures and elevated pressures. *Fuel*. 2018;226:545–554.
33. Arcoumanis C, Bae C, Crookes R, Kinoshita E. The potential of di-methyl ether (DME) as an alternative fuel for compression-ignition engines: a review. *Fuel*. 2008;87(7):1014–1030.
34. Vinkeloe J, Zander L, Szeponik M, Djordjevic N. Tailoring the temperature sensitivity of ignition delay times in hot spots using fuel blends of dimethyl ether, methane, and hydrogen. *Energy Fuels*. 2020;34(2):2246–2259.
35. Brabbs TA, Belles FE. *Contact-surface tailoring in real shock tubes*. Technical report, Levis Research Center, Cleveland, OH; 1965.
36. Amadio AR, Crofton MW, Petersen EL. Test-time extension behind reflected shock waves using CO_2–He and C_3H_8–He driver mixtures. *Shock Waves*. 2006;16(2):157–165.
37. Hong Z, Davidson DF, Hanson RK. Contact surface tailoring condition for shock tubes with different driver and driven section diameters. *Shock Waves*. 2009;19(4):331–336.
38. Synotech. TN-401: Optimale Messergebnisse beim Einsatz piezoelektrischer Druckaufnehmer.
39. Djordjevic N, Rekus M, Vinkeloe J, Zander L. Shock tube and kinetic study on the effects of CO_2 on dimethyl ether autoignition at high pressures. *Energy Fuels*. 2019;33(10):10197–10208.
40. Sheinson RS, Williams FW. Chemiluminescence spectra from cool and blue flames: electronically excited formaldehyde. *Combust Flame*. 1973;21(2):221–230.
41. Hwang W, Dec JSjöberg M. Spectroscopic and chemical-kinetic analysis of the phases of HCCI autoignition and combustion for single- and two-stage ignition fuels. *Combust Flame*. 2008;154(3):387–409.
42. Vandersickel A, Hartmann M, Vogel K, et al. The autoignition of practical fuels at HCCI conditions: high-pressure shock tube experiments and phenomenological modeling. *Fuel*. 2012;93:492–501.
43. Mayo MP, Boehman André L. Ignition behavior of biodiesel and diesel under reduced oxygen atmospheres. *Energy Fuels*. 2015;29(10):6793–6803.
44. Goodwin DG, Moffat HK, Speth RL. Cantera: an object-oriented software toolkit for chemical kinetics, thermodynamics, and transport processes. http://www.cantera.orgVersion 2.3.0; 2017.
45. Hairer E, Wanner G. Stiff differential equations solved by Radau methods. *J Comput Appl Math*. 1999;111(1):93-111.
46. Heufer KA, Olivier H. Determination of ignition delay times of different hydrocarbons in a new high pressure shock tube. *Shock Waves*. 2010;20(4):307–316.
47. Nativel D, Fikri M, Lipkowicz J T, et al. Reflected-shock nonidealities in shock tubes: the impact of the facility-dependent effects over a wide range of pressures and Mach numbers. In: *27th ICDERS*. Beijing; 2019.
48. Petersen EL. *A shock tube and diagnostics for chemistry measurements at elevated pressures with application to methane ignition* (PhD thesis). Stanford University; 1998.
49. Rossmann T. A Simple wave-tracking technique for test time calculations in shock tunnels. In, *41st Aerospace Sciences Meeting and Exhibit*. Reno, NV: American Institute of Aeronautics and Astronautics; 2003.
50. Davidson DF, Oehlschlaeger MA, Herbon JT, Hanson RK. Shock tube measurements of iso-octane ignition times and OH concentration time histories. *Proc Combust Inst*. 2002;29(1):1295–1301.
51. Dean AJ, Penyazkov OG, Sevruk KL, Varatharajan B. Autoignition of surrogate fuels at elevated temperatures and pressures. *Proc Combust Inst*. 2007;31(2):2481–2488.
52. Shen H-PS, Vanderover J, Oehlschlaeger MA. A shock tube study of iso-octane ignition at elevated pressures: the influence of diluent gases. *Combust Flame*. 2008;155(4):739–755.
53. Cancino L, Fikri M, Oliveira AM, Schulz C. Measurement and chemical kinetics modeling of shock-induced ignition of ethanol-air mixtures. *Energy Fuels*. 2010;24:2830–2840.
54. Vranckx S, Heufer KA, Lee C, et al. Role of peroxy chemistry in the high-pressure ignition of *n*-butanol–experiments and detailed kinetic modelling. *Combust Flame*. 2011;158(8):1444–1455.
55. Ramirez Lancheros HP, Fikri M, Cancino LR, Moréac G, Schulz C, Dagaut P. Autoignition of surrogate biodiesel fuel (B30) at high pressures: experimental and modeling kinetic study. *Combust Flame*. 2012;159(3):996–1008.

56. Burke U. *An experimental and modelling study of selected oxygenated biofuels* (Thesis, NUI Galway, Ireland). 2014.
57. Zhang Z, Hu E, Pan L, Chen Y, Gong J, Huang Z. Shock-tube measurements and kinetic modeling study of methyl propanoate ignition. *Energy Fuels*. 2014;28(11):7194–7202.
58. Braun-Unkhoff M, Dembowski J, Herzler J, Karle J, Naumann C, Riedel U. Alternative fuels based on biomass: an experimental and modeling study of ethanol cofiring to natural gas. *J Eng Gas Turbines Power*. 2015;137(9).
59. Mathieu O, Pemelton JM, Bourque G, Petersen EL. Shock-induced ignition of methane sensitized by NO_2 and N_2O. *Combust Flame*. 2015;162(8):3053–3070.
60. AlAbbad M, Javed T, Khaled F, Badra J, Farooq A. Ignition delay time measurements of primary reference fuel blends. *Combust Flame*. 2017;178:205–216.
61. Mathieu OPinzón LT, Atherley TM, Mulvihill CR, Schoel I, Petersen EL. Experimental study of ethanol oxidation behind reflected shock waves: ignition delay time and H_2O laser-absorption measurements. *Combust Flame*. 2019;208:313–326.
62. Shao J, Choudhary R, Davidson DF, Hanson RK, Barak S, Vasu S. Ignition delay times of methane and hydrogen highly diluted in carbon dioxide at high pressures up to 300 atm. *Proc Combust Inst*. 2019;37(4):4555–4562.
63. Zhang J, Hu E, Pan L, Zhang Z, Huang Z. Shock-tube measurements of ignition delay times for the ethane/dimethyl ether blends. *Energy Fuels*. 2013;27(10):6247–6254.
64. BIPM, IEC, IFCC, et al. Evaluation of measurement data – guide for the expression of uncertainty in measurement. JCGM 100:2008. 2008.
65. Davidson DF, Hanson RK. Real gas corrections in shock tube studies at high pressures. *Isr J Chem*. 1996;36(3):321–326.
66. Kogekar G, Karakaya C, Liskovich GJ, Oehlschlaeger MA, DeCaluwe SC, Kee RJ. Impact of non-ideal behavior on ignition delay and chemical kinetics in high-pressure shock tube reactors. *Combust Flame*. 2018;189:1–11.
67. Zhou C-W, Li Y, Burke U, et al. An experimental and chemical kinetic modeling study of 1,3-butadiene combustion: ignition delay time and laminar flame speed measurements. *Combust Flame*. 2018;197: 423-438.
68. Fischer SL, Dryer FL, Curran HJ. The reaction kinetics of dimethyl ether. I: high-temperature pyrolysis and oxidation in flow reactors. *Int J Chem Kinet*. 2000;32(12):713–740.
69. Curran HJ, Fischer SL, Dryer FL. The reaction kinetics of dimethyl ether. II: low-temperature oxidation in flow reactors. *Int J Chem Kinet*. 2000;32(12):741–759.
70. Kaiser EW, Wallington TJ, Hurley MD, et al. Experimental and modeling study of premixed atmospheric-pressure dimethyl ether-air flames. *J Phys Chem A*. 2000;104(35):8194-8206.
71. Zhao Z, Chaos M, Kazakov A, Dryer FL. Thermal decomposition reaction and a comprehensive kinetic model of dimethyl ether. *Int J Chem Kinet*. 2008;40(1):1–18.
72. Gillespie FR. *An experimental and modelling study of the combustion of oxygenated hydrocarbons* (PhD thesis). Galway: National University of Ireland; 2014.
73. Prince JC, Williams FA. A short reaction mechanism for the combustion of dimethyl-ether. *Combust Flame*. 2015;162(10):3589-3595.
74. Hu E, Zhang Z, Pan L, Zhang J, Huang Z. Experimental and modeling study on ignition delay times of dimethyl ether/propane/oxygen/argon mixtures at 20 bar. *Energy Fuels*. 2013;27(7):4007–4013.
75. Metcalfe WK, Burke SM, Ahmed SS, Curran HJ. A hierarchical and comparative kinetic modeling study of C1-C2 hydrocarbon and oxygenated fuels. *Int J Chem Kinet*. 2013;45(10):638-675.
76. Li Y, Zhou CW, Somers KP, Zhang K, Curran HJ. The oxidation of 2-butene: a high pressure ignition delay, kinetic modeling study and reactivity comparison with isobutene and 1-butene. *Proc Combust Inst*. 2017;36(1):403–411.
77. Zhou CW, Li Y, O'Connor E, et al. A comprehensive experimental and modeling study of isobutene oxidation. *Combust Flame*. 2016;167:353–379.
78. Burke U, Metcalfe WK, Burke Sinead M, Heufer K. Alexander, Dagaut P, Curran Henry J. A detailed chemical kinetic modeling, ignition delay time and jet-stirred reactor study of methanol oxidation. *Combust Flame*. 2016;165:125–136.
79. Burke SM, Metcalfe W, Herbinet O, et al. An experimental and modeling study of propene oxidation. Part 1: speciation measurements in jet-stirred and flow reactors. *Combust Flame*. 2014;161(11):2765–2784.
80. Burke SM, Burke U, McDonagh R, et al. An experimental and modeling study of propene oxidation. Part 2: ignition delay time and flame speed measurements. *Combust Flame*. 2015;162(2):296–314.
81. Kéromnès A, Metcalfe WK, Heufer KA, et al. An experimental and detailed chemical kinetic modeling study of hydrogen and syngas mixture oxidation at elevated pressures. *Combust Flame*. 2013;160(6):995–1011.
82. Uygun Y, Ishihara S, Olivier H. A high pressure ignition delay time study of 2-methylfuran and tetrahydrofuran in shock tubes. *Combust Flame*. 2014;161(10):2519–2530.
83. Javed T, Badra J, Jaasim M, et al. Shock tube ignition delay data affected by localized ignition phenomena. *Combust Sci Technol*. 2017;189(7):1138–1161.
84. Laich AR, Ninnemann E, Neupane S, et al. High-pressure shock tube study of ethanol oxidation: ignition delay time and CO time-history measurements. *Combust Flame*. 2020;212:486–499.
85. Ninnemann E, Pryor O, Barak S, et al. Reflected shock-initiated ignition probed via simultaneous lateral and endwall high-speed imaging with a transparent, cylindrical test-section. *Combust Flame*. 2020.

SUPPORTING INFORMATION

Additional supporting information may be found online in the Supporting Information section at the end of the article.

How to cite this article: Zander L, Vinkeloe J, Djordjevic N. Ignition delay and chemical–kinetic modeling of undiluted mixtures in a high-pressure shock tube: Nonideal effects and comparative uncertainty analysis. *Int J Chem Kinet*. 2020;1–27. https://doi.org/10.1002/kin.21469